

# Monitoring Atmospheric Dust Spring Activity at High Southern Latitudes on Mars using OMEGA

S. Douté<sup>1</sup>

<sup>1</sup>*Institut de Planétologie et d'Astrophysique de Grenoble (IPAG), France  
(sylvain.doute@obs.ujf-grenoble.fr Phone: +33 4 76 51 41 71 Fax +33 4 76 51 41 46)*

---

## Abstract

This article presents a monitoring of the atmospheric dust in the south polar region during spring of martian year 27. Our goal is to contribute to identifying the source regions and to understanding lifting as well as transport mechanisms in relation with the seasonal ice regression and the dynamics of the atmosphere. This is of paramount importance since local dust storms generated in this region sometimes grow to global proportions. The imaging spectrometer OMEGA on board Mars Express has acquired the most comprehensive set of observations to date in the near-infrared (0.93–5.1 microns) of the southern high latitudes of Mars from mid-winter solstice ( $L_s=110^\circ$ , December 2004) to the end of the recession at  $L_s=320^\circ$  (November 2005). We use an original method presented in the companion paper in order to retrieve the optical depth of the atmospheric dust above mineral surfaces at a reference wavelength of one micron. The method is applied on a time series of OMEGA images acquired between  $L_s=220^\circ$  and  $L_s=280^\circ$  in conjunction with a complementary treatment of the seasonal cap. As a result the aerosol optical depth (AOD) is mapped and binned at a spatial resolution of  $1.0^\circ \cdot \text{pixel}^{-1}$  and with a mean period of AOD sampling ranging from less than two sols for latitudes higher than  $80S^\circ$  to approximately six sols at latitudes in the interval  $65\text{--}75S^\circ$ . We then generate and interpret time series of orthographic mosaics depicting the spatio-temporal distribution of the seasonal mean values, the variance and the local time dependence of the AOD. We conclude that two mechanisms play a major role for lifting and transporting

efficiently mineral particles and create dust events or storms: (i) nighttime katabatic winds at locations where a favourable combination of frozen terrains and topography exists (ii) daytime mesoscale thermal winds at the edge of the cap when the defrosting area is sufficiently narrow. As regards to the source regions around the cap, the most productive sector spans longitudes 180-300°E around  $L_S \approx 250^\circ$ . Later ( $L_S \approx 267^\circ$ ) the cryptic sector becomes the most productive while the longitude sector 300-60°E remain moderately dust-generative. Inside the seasonal cap, pulsating advection of dust at high altitude from the lower active latitudes is the main origin of the increase of the seasonal atmospheric opacity around  $L_S \approx 235^\circ$ , then  $L_S \approx 275^\circ$ . Our work calls for new simulations of the martian surface-atmosphere dynamics at mesoscales to reproduce the observations and confirm the interpretations.

*Keywords:* Mars; South Pole; Atmosphere; Dust; OMEGA.

---

## Introduction

The southern high latitudes of Mars are of great interest in spring and summer because of their role in the dust cycle. Local dust storms generated in this region sometimes develop to global storms, and a prominent dust collar encircles the polar cap. Several experiments aboard orbiters have recently contributed to elaborate and refine this picture.

The TES and MOC instruments of Mars Global Surveyor have provided a systematic, Sun-synchronous, and regular record of dust activity in the south polar region. [Toigo et al. \(2002\)](#); [Imamura and Ito \(2011\)](#) produced global maps of dust distribution by integrating TES individual 9  $\mu\text{m}$  optical depth measurements averaged over a 5°-Ls period (respectively 10°-Ls) and binned in 5x5° boxes (respectively 5x10°, latitude, longitude). Both sets of maps depict very distinct space and time patterns of activity around the polar cap edge for the first common Martian Year (MY) 24. These seasonal trends are sometimes in contradiction. For the following Martian year 25 and 26, [Imamura and Ito \(2011\)](#) report a great stability of the dust opacity disturbance compared to MY

24. On the other hand Color MOC wide angle images were mosaicked together by [Toigo et al. \(2002\)](#) to produce daily global maps. Such snapshots show very dynamic dust activity near the edge of the retreating south seasonal ice cap throughout mid and late southern spring, then a decline going to midsummer. Thermal mapping of dust by TES is limited to regions where the temperature and thus the emitted signal are sufficiently high, thus precluding the monitoring of the seasonal polar cap itself. Visible MOC snapshots are limited in time coverage and do not provide quantitative values of dust opacity.

The imaging spectrometer OMEGA aboard Mars Express allowed to overcome these limitations since it acquired a comprehensive set of global observations in the near-infrared (0.93–5.1 microns) of the southern high latitudes of Mars in spring and summer. A detailed study of the contribution of water ice aerosols to the OMEGA dataset is provided by [Langevin et al. \(2007\)](#). This study is based on the water ice absorption bands at 1.5, 2, and 3  $\mu\text{m}$ . In 2005 (MY 27) from mid-spring to mid summer most OMEGA observations are nearly free of water ice either as aerosols or on the surface of the southern seasonal cap. [Vincendon et al. \(2008\)](#) performed the mapping of the optical depth of dust aerosols above areas of the south polar cap constituted of pure ice as a function of Ls for dates when the contribution of water ice aerosols can be neglected. The average trend of the temporal evolution is a low optical depth between Ls = 180° and Ls = 250° ( $\tau(2.6 \mu\text{m}) = 0.1\text{--}0.2$ ), an increase of atmospheric dust activity observed between Ls = 250° and Ls = 270° ( $\tau(2.6 \mu\text{m}) = 0.3\text{--}0.6$ ), and then a decrease up to Ls = 310°. [Vincendon et al. \(2008\)](#) observed rapid time variations which are specific to a given location in conjunction to large spatial variations of the optical depth observed over scales of a few tens of kilometres.

Monitoring of dust activity in the high southern latitudes by the previous experiments was accompanied by an important effort in modelling and simulation in order to interpret the observations in terms of processes. The results of general circulation models (GCM) suggest that non convective wind stress lifting produces the peak in the atmospheric dust opacity during southern spring and summer and that convective (dust devil) lifting is responsible for the back-

ground opacity during other seasons ([Basu et al., 2004](#); [Kahre et al., 2006](#)). However the coarse spatial resolution achieved by GCM limits our understanding, fostering specific simulations conducted at mesoscales. The main picture that emerges from the latter studies is that flows capable of lifting dust from the surface can be achieved by a variety of conditions, the most likely being cap edge thermal contrasts ([Toigo et al., 2002](#)) but also topography ([Siili et al., 1999](#)). Regional or synoptic baroclinic instabilities as well as vertical convection in the boundary layer could also play a role ([Imamura and Ito, 2011](#)). These conditions as well as dust loading itself in the atmosphere can interfere constructively or destructively.

More details regarding these investigations are given in relation to our own work in Section [4.5](#).

The previous compilation of observations and simulations show that some uncertainties and opened questions remain regarding dust activity in the high southern latitudes. First [Toigo et al. \(2002\)](#); [Imamura and Ito \(2011\)](#) indicate different area where the mean atmospheric dust loading is well above background levels for the same MY 24. Such discrepancy entails an uncertainty on the location of the main source regions as a function of time. Second, and in relation to the latter comment, the relative importance and interaction of the expected mechanisms for dust lifting has not yet been clearly established. Third dust activity around and inside the seasonal cap has so far been studied separately, using TES and OMEGA data respectively. A more integrated vision could be of paramount importance to investigate the possible negative feedback between dust loading and atmospheric temperature contrast across the cap edge. Finally the main frequency of dust cloud generation and the time they take to dissipate are also apparently inconsistent when examining the results of [Toigo et al. \(2002\)](#) and [Imamura and Ito \(2011\)](#): daily as opposed to every 10-20 sols; a few hours as opposed to 10 sols. Could that be reconciled?

In this paper we bring some new insights about dust activity in the southern polar region by monitoring the dust both inside and around the seasonal cap based on the OMEGA dataset acquired during MY 27. At the same time, special

attention is paid to the exact characteristics of the cap edge based on the work of Schmidt et al. (2009). The mapping of the optical depth of atmospheric dust in the near infrared above mineral surfaces is made possible by the development of a new method that is proposed in a companion paper and that is shortly described in Section 1. Allied to the complementary method by Vincendon et al. (2008), it is applied to analyse the time series of OMEGA observations thus producing hundred of opacity maps. The latter are integrated into a common geographical grid and processed by a special data procedure so as to generate a time series of mosaics. The mosaics depict the seasonal dust loading as well as the day-to-day variability and local time dependence of the dust optical depth according to solar longitude (Section 2). The mosaics are fully described and examined in Section 3. As a result a synthetic view of dust activity in the south polar atmosphere in mid spring to early summer is established and discussed in Section 4. Finally, in Section 5, the main points of our study are summarised.

## 1. Methods for retrieving the optical depth

### 1.1. Above ice free surfaces

In summary (see companion paper for more details) the first method that we operate is based on a parametrisation of the radiative coupling between atmospheric particles and gas that determines, with local altimetry and the meteorological situation, the absorption band depth of gaseous CO<sub>2</sub>. The coupling depends on (i) acquisition geometry (ii) type, abundance, and vertical distribution of the particles (iii) surface albedo. All the previous parameters are assumed to be known from ancillary data or previous studies, except the dust aerosol integrated abundance and surface albedo. Information about the first quantity can be reduced to one value of AOD at a reference wavelength of 1 μm  $\tau_{aer}^{k_0}$  (channel  $k_0$ ) if the intrinsic optical properties of the particles are known (Vincendon et al., 2008; Wolff et al., 2009). For each spectro-pixel of an OMEGA image, we compare the depth of the 2 μm absorption band of gaseous CO<sub>2</sub> that we estimate from two spectra. On the one hand from the observed spectrum when possible, i.e. for surfaces spectrally dominated by minerals or

water ice, even though the procedure can be extended for spectra showing moderate but saturated  $2\text{ }\mu\text{m}$  CO<sub>2</sub> ice absorption band such as in the outer part of the seasonal cap. On the other hand from a transmission spectrum through the atmospheric gases alone calculated ab-initio using a Line-By-Line radiative transfer model and climatic data. This leads to a precious new observable that directly depends on the aerosol optical depth (AOD). Combining the former with the reflectance factor deep into the  $2\mu\text{m}$  band we evaluate, by iterative radiative transfer inversion, the AOD  $\tau_{aer}^{k0}$  and the surface Lambertian albedo  $A_{surf}^k$ .

### *1.2. Above surfaces constituted by pure CO<sub>2</sub> ice.*

The second method by [Vincendon et al. \(2008\)](#) is complementary since it is restricted to area where CO<sub>2</sub> deposits are not contaminated by dust and water, i.e. above most places of the seasonal cap except the cryptic sector and close to the sublimation front where sub-pixel spatial mixing of ice-covered and ice-free surfaces is observed. The mapping is based on the assumption that the reflectance in the  $2.64\text{ }\mu\text{m}$  saturated absorption band of the surface CO<sub>2</sub> ice is mainly due to the light scattered by aerosols. The atmospheric CO<sub>2</sub> (respectively H<sub>2</sub>O) gas absorption at  $2.7$  (respectively  $2.6\text{ }\mu\text{m}$ ) has negligible impact. In this case the reflectance factor varies monotonically as a function of the optical depth for a given set of photometric angles. Therefore, the optical depth can be unambiguously determined by comparing the observed reflectance factor at  $2.64\text{ }\mu\text{m}$  with a reference look-up table. A method for selecting pixels free of dust contamination has been derived from the relationship between the observed reflectance factor at  $1.08\text{ }\mu\text{m}$  and the optical depth modelled from the reflectance at  $2.6\text{ }\mu\text{m}$ . Correlation of low frequency spatial variations of optical depth with altitude can be modelled with a well-mixed dust atmospheric component with a scale height of  $11\text{ km}$ .

As a conclusion the two methods are complementary since our approach specifically treats pixels occupied by purely mineral/H<sub>2</sub>O surfaces or by icy deposits contaminated by a large amount of dust. Conversely the method of [Vincendon](#)

[et al. \(2008\)](#) is restricted to area where CO<sub>2</sub> deposits are not contaminated by dust and water. Their common strength relies in the ability to provide estimation of the AOD for each pixel of a single image, i.e. at a fixed geometry. As regards the uncertainties, limitations on the knowledge of the optical properties of aerosols will induce a possible, systematic, and uniform bias in the maps. For the first method, empirical tests have shown that this bias is likely small since the gas-aerosol coupling is weakly dependent on the single scattering albedo and the phase function of the aerosols in the range of models proposed by authors in the last few decades. For the second method, the multiplication of all the optical depth maps by a factor ranging from 1 to 1.36 could be expected. In both cases the assumption of a lambertian surface has little effect on the results. Otherwise the relative uncertainty linked with stochastic errors in the measurements or in the modelling is of the order of 10%.

## 2. Analysis of a time series of OMEGA observations

### 2.1. The dataset

The imaging spectrometer OMEGA on board Mars Express has acquired a comprehensive set of observations in the near-infrared (0.93-5.1 microns) in the southern high latitudes of Mars from mid-winter solstice (Ls=110°, December 2004) to the end of the recession at Ls=320° (November 2005) of martian year MY=27. These observations provide a global coverage of the region with a time resolution ranging from 3 days to one month and a spatial resolution ranging from 700m to 10 km/pixel. We refer to [Langevin et al. \(2007\)](#) for a complete description. We have systematically processed a subset of 284 observations from L<sub>S</sub>=220° to 280° by using the two complementary methods of Section 1. As a result, we obtain a series of corresponding  $\tau_{aer}^{k0}$  maps in the image space (optical depth  $\tau_{aer}$  of the atmospheric dust at a reference wavelength of one micron) that were de-trended according to a reference altitude of 0 km in order to correct for changes due solely to varying atmospheric height because of topography:

$$\tau_{det}^{k0} = \tau_{aer}^{k0} \exp(h/H_{scale}) \quad H_{scale} = 11\text{km}$$

The timescale between two maps that partially overlap is frequently between  $0.5^\circ$  and  $1^\circ$  of Ls.

## 2.2. Integrating the AOD maps into a common geographical grid

These maps were independently integrated onto a common geographical grid generated from the Hierarchical Equal Area isoLatitude Pixelization (Healpix, <http://healpix.jpl.nasa.gov>, (Górski et al., 2005)) of Mars southern hemisphere at different spatial resolutions. Such an integration makes it easy to create a mosaic at a given date or to build a time evolution curve at a given location. The resolution of the grid is expressed by the parameter  $N_{side}$  which defines the number of divisions along the side of a base-resolution bin that is needed to reach a desired high-resolution partition. The total number of bins equal to  $N_{pix} = 12 \times N_{side}^2$ . Two built-in properties of Healpix - equal areas of discrete elements of partition, and Iso-Latitude distribution of discrete area elements on the sphere - make it easy to map any point of coordinate ( $lat, long$ ) into the corresponding bin. The latter can also be tagged and addressed by a single integer. If one considers in addition a partition of time according to discrete solar longitudes - those of the observations - any space-time data can be conveniently stored into a two dimensional array (the Primary Integrated Data Array, PIDA). Its X dimension corresponds to the bin number and its Y dimension corresponds to the time index. Consequently the  $\tau_{det}^{k0}$  maps - each corresponding to a given image and thus date - are integrated, one at a time, by mapping all the pixels where the AOD evaluation has succeeded to the appropriate line of the array. In case several pixels fall into the same bin, their values are averaged. After completion of the operation, the whole collection of maps has been integrated into a common geographical grid providing a mean period of AOD sampling for each bin that depends basically on the latitude. As illustrated by Figure 1 in the case  $N_{side}=64$  ( $1.0^\circ.\text{pixel}^{-1}$ ) the mean period ranges from less than two sols for latitudes higher than  $80^\circ\text{S}$  to approximately six sols at latitudes in the interval  $65\text{--}75^\circ\text{S}$ . An additional dimension can be optionally added to the PIDA by considering the local time of acquisition for each pixel.

Then a division of the martian sol into three equal Local Time (LT) intervals is adopted: 0-6, 6-12, and 12-18. The interval 18-24 is abandoned since it is only moderately populated by the OMEGA spatio-temporal points of acquisition.

### *2.3. Describing time evolutions*

Figure 2 shows as an example the time evolution of the AOD for a bin chosen into the anticryptic longitude sector (see definition in Section 3.1). It was plotted by extracting a column of the PIDA. A noticeable day to day variability (one data point to the next) can be immediately noted. This can be expected for a very dynamic environment such as the polar atmosphere in spring and beginning of summer. Variability could also be accounted for by random errors that affect the AOD retrieval but, with a theoretical root mean square of the order of  $\approx 0.05$ , they can only explain a part of it. A gap between  $L_S=228^\circ$  and  $L_S=235^\circ$  and irregularities in the sampling are also evident in the plot. Indeed coverage of the area by the OMEGA sensor had necessary some limitations due to orbital characteristics, planning constraints, and episodic OMEGA malfunctions. To mitigate the difficulties induced by the previous factors on the analysis, we consider that any of these temporal signals consists of two contributions: a mean trend of  $\tau_{det}^{k0}$  versus time, i.e. the baseline, and a highly variable component, i.e. the variability around the baseline. The former can be calculated by regression provided enough data points are available. The latter is just the difference between the original signal and the mean trend. We now define the baseline of any time evolution curve as the curvilinear frontier that divides longitudinally the elongated cloud of data points into two approximately equal parts (continuous line in Figure 2). The typical local curvature of the baseline is controlled by a characteristic time scale that is fixed at  $\Delta L_s=5^\circ$ . Such parameter acts as a threshold that separates what we consider to be a seasonal trend from what is the day-to-day variability.

In order to calculate the baseline, we use Support Vector Machine (SVMs) Vapnik (1998) a popular machine learning method for classification, regression, and other learning tasks. Traditional polynomial fit is not suited to model the

mean trend with its typical ups and downs which will require using high orders. In addition SVM-based regression allows us to control the characteristic time scale of the modelling. Consider a set of training points,  $\{(\mathbf{x}_1, y_1), \dots, (\mathbf{x}_l, y_l)\}$  where  $x_i \in \mathbb{R}^n$  is a feature vector,  $y_i \in \mathbb{R}^1$  is the target output, and  $l$  is the number of data points available. Under two given parameters  $C > 0$  and  $\epsilon > 0$  and the choice of a kernel function  $K$ , the standard form of the Support Vector Regression ( $\epsilon$ -SVR) is:

$$\begin{aligned} \min_{\alpha, \alpha^*} \quad & \frac{1}{2} (\alpha - \alpha^*)^T \mathbf{Q} (\alpha - \alpha^*) + \epsilon \sum_{i=1}^l (\alpha_i + \alpha_i^*) + \sum_{i=1}^l y_i (\alpha_i - \alpha_i^*) \\ \text{subject to} \quad & \mathbf{e}^T (\alpha - \alpha^*) = 0, \\ & 0 \leq \alpha_i, \alpha_i^* \leq C, \quad i = 1, \dots, l, \end{aligned}$$

where  $Q_{ij} = K(\mathbf{x}_i, \mathbf{x}_j)$ . The solutions of the previous optimisation problem is expressed in the form of  $l$  support vectors  $\alpha_i - \alpha_i^*$  and a constant  $b$  such that the  $\mathbb{R}$ -valued approximate regression function is:

$$f(\mathbf{x}) = \sum_{i=1}^l (-\alpha_i + \alpha_i^*) K(\mathbf{x}_i, \mathbf{x}) + b$$

The self-adaptation of  $\epsilon$ -SVR to any kind of curvilinear frontier is a decisive advantage in our case. For implementation of the regression we use the library of support vector machine routines LIBSVM ([Chang and Lin, 2011](#)), one of the most widely acclaimed SVM package. We choose a radial basis function:  $K(\mathbf{x}_i, \mathbf{x}_j) = \exp(-\gamma \|\mathbf{x}_i - \mathbf{x}_j\|^2)$  where the parameter  $\gamma$  controls the width of the function and is directly related to the characteristic time scale  $\gamma = 2\Delta L_s$ . Regarding our regression, it should be noted that the feature vectors reduce to scalars (solar longitudes) that are linearly mapped into  $[0, 1]$ . The boundaries of the previous interval correspond respectively to the minimum and maximum solar longitude considered in our study. The parameter  $\epsilon$  appears in the cost function and accommodates the dispersion of the data. In our case it is fixed at 0.05. Finally parameter  $C$  is a regularisation term that is usually set to 1.0 by default. The LIBSVM routine for  $\epsilon$ -SVR directly outputs  $\alpha - \alpha^*$  and  $b$  allowing

us to build the model of the mean trend of  $\tau_{det}^{k0}$  versus time for any bin of the HEALPix grid for which enough points are available and sufficiently distributed in the period of interest. The bins for which these criteria are satisfied fall predominantly above the 70<sup>th</sup> parallel, the precise number depending only slightly on the chosen spatial resolution of the grid. We find that  $N_{side}=64$  is the best compromise between the spatial resolution and the number of curves to model. Having a model for the seasonal trend in the form of a regression function allows to fill the gaps in the PIDA that is then restricted to the baseline component (Modified Integrated Data Array, MIDA). Nevertheless this is done at the expense of the spatial coverage as explained above.

#### *2.4. Generating time series of mosaics*

Facilities associated to healpix provide a means to represent each line of the PIDA or MIDA on a geographical map according to different projections. In particular the orthographic projection is the most suited among those available for the representation of the southern polar region of Mars. Prior to the mapping of the MIDA, we average along the Y dimension of the array all the valid values falling in a given solar longitude interval (of width 10° for the first two mosaics and then 2° for the following): L<sub>S</sub>=220-230°, 230-240°, 240-242°, and so on. In addition, subsequently to the mapping, we superpose on the map the position of the Seasonal South Polar Cap (SSPC) crocus lines as determined by [Schmidt et al. \(2009\)](#) at the beginning of each time interval of interest. The outer (respectively inner) crocus line is defined as the set of locations that contain for a given date a CO<sub>2</sub> ice coverage ≈ 1% (respectively ≈ 99%). The crocus lines thus describe the local structure of the edge of CO<sub>2</sub> frost deposits that are regressing toward the high latitudes during spring and beginning of summer. As a result we obtain a series of 22 mosaics (at a spatial resolution of  $N_{side}=64$ , i.e. 1.0°.pixel<sup>-1</sup>) that compiles the modelled version of the observations. Discussion of the results will be principally based on the these mosaics . Projections of individual lines of the PIDA (i.e. AOD maps at a spatial resolution of  $N_{side}=1024$ , i.e. 1/16°.pixel<sup>-1</sup> from given OMEGA observations ) are marginally examined

to get some hints about the lowest latitudes and around the cap edge.

### *2.5. Classifying the seasonal trends of $\tau_{det}^{k0}$*

Even though the modelling of the seasonal trend is performed in a pixel-wise manner, the spatial coherency of the time series of mosaics is excellent as can be seen in Figures 3 and 4). Then we may expect that in the MIDA, baselines can be gathered, based on similar shapes, into a limited number of classes. To test this hypothesis the whole collection of baselines is processed by kmeans classification provided by the R statistical package (<http://www.r-project.org/>). The main difficulty to overcome is the prior evaluation of the class number  $N_{class}$ . For that purpose, several runs of the kmeans routine are conducted independently with an increasing value for this unknown input parameter. Then statistical tests Sugar and James (2003) are performed through the generation of a likelihood function depending on  $N_{class}$  and peaking at the most likely value  $\hat{N}_{class}$  for the previous parameter. We found  $\hat{N}_{class}=4$  though with a poor separability of the classes (inter-class variance only accounts for 32 % of the total variance of the data). This is to be expected when studying atmospheric conditions that transition progressively at the global scale of our investigation from one regime to the next. Nonetheless Figure 5 demonstrates that a good spatial coherency and seasonal baseline separability is achieved for the four classes which boundaries must be considered as indicative only.

### *2.6. Assessing day-to-day variability and spatial heterogeneity*

In Section 2.3 we define the variable component as the difference between the original signal and the mean trend respectively extracted from the PIDA and MIDA for the same (x,y) coordinates. We simply define an estimator of the day-to-day variability magnitude by calculating for each valid healpix bin the root mean square (RMS) of these differences over non-overlapping contiguous intervals of solar longitudes 10° in duration. By mapping the estimator in the geographical space according to the orthographic projection, six mosaics are obtained that indicate the most and least active locations for each time period (Figure 6). The relevance of these mosaics has been checked by comparing

them to conjugated maps indicating the integrated number of original image pixels that falls into each bin of the PIDA for  $L_S=220\text{--}230^\circ$ ,  $230\text{--}240^\circ$ ,  $240\text{--}250^\circ$ ,  $250\text{--}260^\circ$ ,  $260\text{--}270^\circ$ , and  $270\text{--}280^\circ$ . No correlation is found for any of the time periods. As regards to spatial heterogeneity, we perform its assessment over the four spatial regions conjugated to the classes distinguished in the previous Section. We first calculate the root mean square of the variable component over a given region at each date, - time index - of the PIDA. We then obtain four temporal curves at full time resolution that are smoothed by a sliding average operation (width of the window:  $10^\circ L_S$ ). The result is then sampled at the solar longitudes  $225^\circ$ ,  $235^\circ$ ,  $245^\circ$ ,  $255^\circ$ ,  $265^\circ$ , and  $275^\circ$  (Figure 7 lower graph).

Another interesting way of examining the variable component of the dust optical depth is to built Hovmöller diagrams (Figures 9 and 8). These 2D plots present zonal (respectively latitudinal) profiles (horizontal dimension) that are extracted and aligned according to time (vertical dimension) for a series of latitudinal (respectively zonal) bands. The variable component is beforehand averaged over spatio-temporal bins  $2^\circ$  wide in latitude,  $20^\circ$  wide in longitude, and  $2^\circ$  in solar longitude. If cyclic and/or propagating transient events should occur, one may expect coherent structures in these space-time diagrams.

### 3. Trends of atmospheric dust opacity for the high southern latitudes

#### 3.1. Main spatio-temporal units

Figure 5 displays the contours of the four principal spatio-temporal units that have emerged from classifying the collection of seasonal trends followed by the dust optical depth. The first unit roughly spans the area between meridians  $90^\circ\text{E}$  and  $210^\circ\text{E}$  and parallels  $70^\circ\text{S}$  and  $85^\circ\text{S}$ . It corresponds basically to the portion of the southern polar layered deposits (SPLD) known as the “cryptic region” (Kieffer et al., 2000) that is opposite in longitude to the portion occupied by the permanent cap (“anti-cryptic sector”). It is characterised by a steady rise of  $\tau_{det}^{k0}$  from  $\approx 0.3$  at the beginning of the covered period to a maximum  $\approx 1.0$  at  $L_S=270^\circ$ . The rate of increase is moderate for  $230 \lesssim L_s \lesssim 240^\circ$ , before being accentuated. Once passed the maximum, one can observe a noticeable

drop in the curve. Unit 2 is composed basically of two non contiguous area, the most extended being between meridians 210°E and 300°E and parallels 70° and 80°: Parva Planum, Argentera Planum. The eastern most part of the area is actually slightly deported towards the lower latitudes. The least extended area of unit 2 is centred around (78°S,100°E; western part of Promethei Planum). As regards to its temporal behaviour, this unit can be distinguished by a steady rise of  $\tau_{det}^{k0}$  that starts at higher values than unit 1 ( $\approx 0.5$ ), has a significantly lower rate of increase, and reaches a maximum value of  $\approx 0.9$  (at  $L_S=265^\circ$ ). Then  $\tau_{det}^{k0}$  declines to some degree. Unit 3 is quite contiguous even though it displays a complex shape. The major part of it lies principally between longitudes 270°E and 30°E and at latitudes as high as 87°S and as low as 70°S including Dorsa Argentera. It also comprises the area occupied by the so-called Mountain of Mitchell (James et al., 2000) and an “arm” of SPLD around the south permanent cap at longitudes between 120°E and 270°E. The atmospheric opacity of unit 3 is already quite high at the beginning of our period of interest around  $\approx 0.55$ , stays quite constant until  $L_S=240^\circ$ , and increases afterwards up to a maximum of  $\approx 0.75$  at  $L_S=255^\circ$ . Then it decreases down to a minimum of  $\approx 0.6$  at  $L_S=272^\circ$ . Our curve indicates the beginning of a reversal afterwards, but it is not possible to say if it is significant. Finally unit 4 surrounds the quasi totality of unit 3 as a “stripe” passing through (clockwise) the permanent cap and the nearby SPLD, the Argentera Planum, the Sisyphi Planum, and the Dorsa Brevia. A possible relationship between the temporal behaviours of unit 3 and 4 can be noticed. Until  $L_S=240^\circ$ , the dust opacity remains basically at the same level ( $\approx 0.55$ ) despite moderate rise for unit 4. Afterwards the two baselines of temporal evolution are nearly in opposition of phase one reaching its minimum ( $\approx 0.5$  at  $L_S=250^\circ$  for unit 4) when the other reaches its maximum and the other way around ( $\approx 0.8$  at  $L_S=275^\circ$  for unit 4).

### *3.2. Regional traits of AOD activity*

The spatio temporal units with their distinct temporal signatures are the summarised expression of the dust loading of the atmosphere at the time scale

of  $\Delta L_s = 5^\circ$  throughout the polar latitudes. This loading is depicted with more details by the time series of mosaics built from the MIDA (explained in Section 2.4 and displayed in Figures 3 and 4). In addition one can appreciate the possible effects of the regressing seasonal deposits by looking at the simultaneous displacement of the inner and outer crocus lines. When the “cryptic” region is entirely covered by CO<sub>2</sub> frost ( $220 \lesssim L_s \lesssim 230^\circ$ ), the overlying atmosphere AOD is the lowest of the entire seasonal cap. As the inner crocus line progresses through the region toward the high latitudes - faster than in any other longitude sectors - patches of more dusty atmosphere appear above the area that are just defrosted. By  $L_S = 254^\circ$ , only the central part of the cryptic region displays AOD values below  $\approx 0.5$ . Superimposed on the mean behaviour of steadily increasing opacity as noted above, we observe by  $L_S = 262^\circ$  the emergence of a regional AOD maximum centred at (80°S, 165°E) that grows in value and spatial extent and reaches its height at  $L_S = 272\text{--}274^\circ$ , and starts to disappear afterwards but not completely. Thus this regional enhancement of dust opacity is present for at least  $\approx 20$  days. In the most western part of the cryptic region around the location (78°S, 100°E; western part of Promethei Planum), there is an area of the same sort but that has been active even earlier ( $L_S = 230^\circ$ ). As result it is classified as belonging to unit 2 rather than to unit 1 and corresponds to the second component area of the former. Unit 2 which falls principally in the “anti-cryptic” sector sees in many places a rise of atmospheric opacity since the beginning, i.e. even before the passage of the crocus lines. Defrosting has only a modest influence on the rate of increase (quite stable) and several regional maxima’s develop, the most important one being along longitude 270°E and migrating towards the higher latitudes by  $\approx 5^\circ$  between  $L_S = 252^\circ$  and  $L_S = 280^\circ$ . Unit 3 is the portion of the seasonal cap that also shows relatively high and growing values of the overlying atmosphere AOD at least for  $240 \lesssim L_s \lesssim 255^\circ$ . However contrary to unit 2, this trend then starts to reverse and the crossing of the inner crocus line - thus the subsequent prevalence of ice-free terrains - are correlated with a substantial apparent clearing of the atmosphere. At the end of the period of interest we observe a regional minimum of dust opacity around

( $75^{\circ}\text{S}, 330^{\circ}\text{E}$ ; Dorsa Argentera). At the lowest latitudes that we cover in the “anti-cryptic” sector an early increase of AOD (modest in amplitude) followed by a decline is also observed linked to the passage of the inner crocus line. After  $L_S=250\text{-}270^{\circ}$  with the passage of the outer crocus line, the AOD starts to recover reaching  $\approx 0.5$  to 1 at the end of the period. Curiously, even though the region of the permanent cap does not experience the crossing of the crocus lines, it displays a very comparable behaviour and thus also is classified in unit 4. Nevertheless this might just be a coincidence. To conclude one can note that, starting at  $L_S=262\text{-}264^{\circ}$ , the progressing transition zone between the inner and outer crocus lines is accompanied by a nearly continuous strip of relatively low AOD values ( $\approx 0.5\text{-}0.6$ ). Such a propagating perturbation explains the major characteristics of the temporal behaviour of units 3 and 4 and their opposition of phase.

### *3.3. Studying day-to-day variability and spatial heterogeneity*

In Section 2.6 an estimator of the magnitude of the day-to-day variability is put forward and mapped at a resolution of  $1.0^{\circ}.\text{pixel}^{-1}$  for six non-overlapping contiguous intervals of solar longitudes  $10^{\circ}$  in duration ( $220\text{-}230^{\circ}$ ,  $230\text{-}240^{\circ}$ ,  $240\text{-}250^{\circ}$ ,  $250\text{-}260^{\circ}$ ,  $260\text{-}270^{\circ}$ , and  $270\text{-}280^{\circ}$ ). The area where the resulting mosaics admit meaningful values is more restricted in general than the area for which we have models of the mean trend of  $\tau_{det}^{k0}$  versus time. Indeed calculation of the estimator requires even more OMEGA observations per time intervals than for the model. Nevertheless this is not a limiting factor for studying the day-to-day variability above  $70^{\circ}\text{S}$  latitude. For  $220 \lesssim L_s \lesssim 230^{\circ}$  the variability is low ( $\approx 0.07$ ) throughout the SSPC with a few exceptions. Then, passed  $L_S \approx 230^{\circ}$ , the variability begins to rise very significantly (up to 0.3) in the “cryptic” sector at large (longitudes  $60\text{-}240\text{E}^{\circ}$ ) regardless of the relative position of the considered bin with the inner crocus line. During the next time interval, such signs of intense dynamics have intensified in the previous sector but have also propagated both clockwise and anti-clockwise. In the anti-cryptic sector enhanced values for the variance are confined within the transition zone. Inside

the SSPC only the 0-60°E interval of longitudes remains relatively quiet. Then we reach the period ( $250 \lesssim L_s \lesssim 270^\circ$ ) during which high variability is widespread among all sectors. Finally ( $270 \lesssim L_s \lesssim 280^\circ$ ) the dynamics decreases in intensity especially inside the remaining SSPC and for latitudes below  $\approx 75^\circ\text{S}$ . Figure 7 illustrates the average seasonal evolution of the day-to-day variability (left) and the seasonal evolution of spatial heterogeneity (right) for each of the four units distinguished in Section 2.5. These graphs corroborate the previous examination. Furthermore they reveal that for  $220 \lesssim L_s \lesssim 250^\circ$  each spatio-temporal unit has a very distinct signature. The atmospheric dust cover above the “cryptic” region (unit 1) displays the highest temporal variability in conjunction of being the most spatially segregated. Nevertheless a look at Figure 5 (right) reminds us that the absolute level of AOD is in general relatively lower than anywhere else. At the contrary above the “anti-cryptic” sector including the “Mountains of Mitchell” (unit 3) the dust cover is much more spatially uniform also implying a low day-to-day variability. Units 2 and 4 are intermediate and respect the rough correlation that exists between spatial segregation and activity. After  $L_S \approx 255^\circ$  all units behave comparably to a first approximation.

### 3.4. Tracking local time dependencies

In this section our goal is to characterise local time dependencies of atmospheric optical depth during spring and beginning of summer for the high southern latitudes. In Section 2.2 we mention that an additional dimension can be optionally added to the PIDA by considering the local time of acquisition for each OMEGA pixel. A division of the martian sol into three equal Local Time (LT) intervals is adopted: 0-6, 6-12, and 12-18. Identically to what is described in Section 2.3 we model the mean trend of  $\tau_{det}^{k0}$  versus  $L_S$  although each LT interval is now treated independently. As a result any systematic variations of the AOD linked with the diurnal cycle should be dissociated to the variability associated to random  $\tau_{det}^{k0}$  estimation errors and day-to-day meteorology for example. The drawback of adding the LT dimension is that the number of samples per bin of the HEALPix grid is now much reduced. The

bins for which enough points are available and sufficiently distributed in the period of interest fall predominantly above the 80<sup>th</sup> parallel, the area that was scrutinised the most frequently by OMEGA. Finally the modelling leads to the generation of three MIDA, one per LT interval. Prior to further processing, we average along the Y dimension of each array all the valid values falling in the reference solar longitude intervals:  $L_S=220\text{--}230^\circ$ ,  $230\text{--}240^\circ$ ,  $240\text{--}242^\circ$ , etc. At this point quantifying the spread and the ordering of the triplet of  $\tau_{det}^{k0}$  values ( $B_{0\text{--}6}$ ,  $B_{6\text{--}12}$ ,  $B_{12\text{--}18}$ ) - one per baseline - is performed for each eligible bin and each  $L_S$  range. In addition a better visualisation of the results is achieved by means of a special colour coding. We assign to each bin a distinctive primary hue and a luminosity depending on the ordering of the triplet and on its variance  $var_{LT}$  as follows. Red, magenta, blue, cyan, green, and yellow correspond respectively to the six possible ordering, i.e. permutations, among the three baselines. The luminosity is a continuous real number in the [0,1] interval that is set to  $\min(\sqrt{var_{LT}}/0.22, 1)$ . The denominator of the previous fraction represents three times the standard deviation of  $\sqrt{var_{LT}}$  when doing the statistics on the whole dataset. By mapping our colour coded joint estimators of ordering and variance in the geographical space according to the orthographic projection we obtain a time series of mosaics (Figures 10 and 11). Bright and subdued colours indicate significant, respectively undetectable, LT variability.

At the beginning of the covered period  $L_S=220\text{--}230^\circ$  a clear dichotomy separates the “cryptic sector” of longitudes with high diurnal variance and the “anti-cryptic” sector with much less pronounced values of  $var_{LT}$ . Nevertheless in both cases we observe two regimes:  $B_{6\text{--}12} < B_{0\text{--}6} < B_{12\text{--}18}$  (magenta) in the western part ( $0\text{--}150^\circ\text{E}$ ) and  $B_{12\text{--}18} < B_{6\text{--}12} < B_{0\text{--}6}$  (yellow) in the eastern part ( $150\text{--}300^\circ\text{E}$ ). The remaining area shows no sign of diurnal variability until  $L_S \approx 240^\circ$ . During the period  $230 \lesssim L_s \lesssim 244^\circ$  the portion of unit 1 (see Section 2.5) covered by the map stays predominantly in the yellow regime even though the middle part shows very low values of  $var_{LT}$ . Meanwhile closer to the pole over a quite extended area we rather have  $B_{0\text{--}6} < B_{6\text{--}12} < B_{12\text{--}18}$  (“red” regime). In the interval  $244 \lesssim L_s \lesssim 248^\circ$  a transition can be observed.

Then for  $248 \lesssim L_s \lesssim 262^\circ$  the predominance of the red regime is obvious everywhere except in the sector  $240\text{-}270^\circ\text{E}$  where the ordering remains in the regime  $B_{6\text{-}12} < B_{12\text{-}18} < B_{0\text{-}6}$  (cyan) until  $L_s \lesssim 258^\circ$ . In any case the variance is moderate to low. After  $L_S \approx 264^\circ$  and at least until  $L_S \approx 274^\circ$  the yellow regime returns with quite high diurnal variability over the SPPC and for longitudes  $180\text{-}240^\circ\text{E}$  at the outskirts of the covered area. Past this date no clear spatially coherent trends are visible in the mosaics in terms of ordering nor in terms of spread.

### 3.5. Transient events

We now examine the Hovmöller diagrams aimed at identifying any cyclic or propagating transient events regarding dust optical depth at the time scale of  $\Delta L_s = 5^\circ$  or below. Inside the seasonal cap at latitudes higher than  $\approx 83^\circ\text{S}$  the Hovmöller diagram of Figure 8 ( $L_S$  versus longitude) shows coherent spatio-temporal patterns. Transient rises of dust opacity that span a large range of longitudes occur three times at  $L_S \approx 241$ ,  $254$ , and  $270^\circ$  respectively. Well outside the cap, no clearly structured patterns are visible. We deduce from such a monitoring that either the frequency of OMEGA acquisition was not high enough to pick up the displacement of the dust structures during their lifetime or the latter do not move over large distances. The Hovmöller diagram of Figure 9 ( $L_S$  versus latitude) confirm the existence of three well defined events inside the cap. At contrary, passed the crocus line, no obvious pattern emerges with the possible exception of the longitude bands  $80\text{-}100^\circ\text{E}$  and  $100\text{-}120^\circ\text{E}$ . In these cases we note that positive disturbances span tens of degree in latitude within a  $2^\circ$  interval of solar longitude.

Further insights into the dust activity going on around the cap edge and at lower latitudes emerges from the examination of individual projected AOD maps (Section 2.4). Information provided by the latter is enhanced by providing two companion maps for each observation. In the first, an RGB composition of the TOA martian reflectivity measured by OMEGA at three wavelengths (0.7070, 0.5508, and 0.4760  $\mu\text{m}$ ) is shown. It is stretched so as to make visible

the dust clouds as yellowish hues against mineral surfaces while the seasonal deposits appear completed saturated. In the second map, a colour scale is used to indicate the local time of pixel acquisition. Figures 12 to 14 shows a selection of eight observations out of the initial collection of 284 observations that illustrate different types of representative situations. However the following description is based on the entire collection. In the interval  $L_S \approx 220\text{-}242^\circ$  for which OMEGA provided global scale observations, we first note significant dust opacity's around the cap ( $\tau_{det}^{k0} \approx 0.6\text{-}0.7$ ) on the "morning" side and modest values on the "afternoon" side of the AOD maps (Fig.12b,c). This is corroborated by the visible images (Fig.12a). Then starting around  $L_S \approx 230^\circ$  and lasting at least until  $L_S \approx 240^\circ$  both the AOD maps (Fig.12e) and their visible counterparts (Fig.12d) reveal thick dust clouds mostly in the vicinity of the seasonal cap regardless of the local time (Fig.12f). It is worth mentioning that while the clouds are well outside the cap on the "morning" side, they penetrate well passed the transition zone on the "afternoon" side. After  $L_S \approx 240^\circ$  until the end of the covered period, global observations turn to more frequent but more spatially focused snapshots. The interval  $L_S \approx 242\text{-}252^\circ$  is a period of quiescent activity in the afternoon for the defrosted area of regions 1, 2, and 4a with low to moderate as well as quite homogeneous level of opacity ( $\tau_{det}^{k0} \approx 0.2\text{-}0.5$ , Fig.13b). In the visible such a situation means a clear view of the surface brown features and low TOA reflectivity's (Fig.13a). From at least  $L_S \approx 250^\circ$  to the end of the covered period ( $L_S \approx 280^\circ$ ) many transient events can be spotted around the cap with clear patterns depending on the spatio-temporal unit that this considered. Once passed the crocus line, unit 1 ("cryptic region") presents area of high atmospheric opacity's that persist regardless of the local time. Nevertheless the highest values of  $\tau_{det}^{k0}$  occur more frequently during the second part of the "night" and in the morning than at any other times (Fig.14e,h). In such cases surface features in the visible are subdued behind a diffuse veil of scattering aerosols with relatively elevated TOA reflectivity's (Fig.14d,g). Thick dust clouds can also been encountered occasionally during the afternoon. For regions 2 and 4a the area close to defrosting area undergo locally intense dust activity ( $\tau_{det}^{k0} \approx 1$ - $2$ )

1.5) that are observed rather during the afternoon hours than during the early morning. A typical “storm” is shown in Fig. 14, 1st row. On peculiar example (Fig.13 2nd and 3rd rows) appears to be a long lived event ( $L_S \approx 260\text{--}270^\circ$ ) affecting Unit 4a around the point of coordinates ( $65^\circ\text{S}, 30^\circ\text{E}$ ). Two out of five revealing AOD maps are displayed in Fig.13d,g. High values of dust optical depth coincide in their visible counterparts with brown-reddish hues that show the same temporal behaviour. In this case we may infer the existence of aerosols with different physical properties (e.g. composition or mean diameter) than usual dust. One last observation concerning units 2 and 4a is that the area that had been defrosted for  $\approx 10^\circ$  of solar longitude show low to moderate AOD corresponding to quite clear conditions in the visible images.

#### 4. Discussion

Figure 15 proposes a synthetic view of the principal results obtained in Section 3. The four main spatio-temporal units are followed in parallel according to the solar longitude. A series of indicators - the seasonal trend of  $\tau_{det}^{k0}$  (Section 2.3), the day-to-day variability  $var_{D2D}$  and spatial heterogeneity (Section 2.6), as well as the ordering and spread  $var_{LT}$  of the triplet of baseline values ( $B_{0-6}, B_{6-12}, B_{12-18}$ ) (Section 3.4) are used conjointly in order to get hints about the mechanisms controlling the atmospheric dust activity. In addition we indicate which time interval is concerned by the passage of the crocus lines.

##### 4.1. Unit 1

For unit 1, that well corresponds to the “cryptic” region, we distinguish four successive phases of activity.

In the very early phase of defrosting ( $220 \lesssim L_s \lesssim 240^\circ$ ), the seasonal AOD is the lowest of the entire seasonal cap, and we have  $B_{12-18} < B_{6-12} < B_{0-6}$  (i.e. a “yellow regime”) with dispersed values of  $var_{LT}$ , meaning that, statistically, there is more dust in the atmosphere during the early hours than during the morning and the afternoon with local variations of the spread. For  $220 \lesssim L_s \lesssim 230^\circ$  the mantle of seasonal CO<sub>2</sub> deposits is still quite continuous

and exhibits a very compact texture in the form of a translucent slab (Kieffer et al., 2000). Nonetheless it is then superficially contaminated by a large amount of dust making it barely detectable by its spectral signature in the shortwave infrared (Langevin et al., 2006). The skin-deep contamination is likely due to the functioning of vents triggered by the basal sublimation of CO<sub>2</sub> that escapes the slab as a mixture of gas and entrained dust along fissures (Kieffer et al., 2006). We first put forward the hypothesis that the emitted dust forms low lying dust clouds in the atmosphere that are not detectable by the method we use to retrieve the optical depth (Section 1). The emission would be maximal during daytime because its existence is triggered by solar illumination. Then during the late (18-24LT) and early (0-6LT) hours the dust would diffuse upward in the atmosphere despite its great stability, thus increasing slightly its radiative coupling with the gas. As a result, the AOD that we estimate becomes higher, the apparent amplification being dependant on the effectiveness of the diffusion that varies from one location to the other. Alternatively we put forward a second hypothesis: some powerful winds can be triggered by gravitationally unstable cold air masses, the so-called katabatic winds that hurtle down existing slopes. They are maximum at night hours when the temperature inversion above icy surfaces is the highest (Spiga, 2011; Kauhanen et al., 2008; Siili et al., 1999). These winds likely cause high surface wind stresses lifting the dust that contaminates the ice but at the same time evacuate the dust downstream. Thus they inhibit accumulation, at least upward diffusion, above the region. By the same token we could also explain the fast superficial cleaning undergone by the CO<sub>2</sub> icy deposits at the ground as noted by Langevin et al. (2006) between  $230 \lesssim L_s \lesssim 240^\circ$ . As for the requirement of significant slopes, we find in the area the mouth of two chasma and the south polar layered deposits display their most pronounced scarps down to the surroundings plains. Considering this series of arguments we favour the katabatic mechanism (KW) for  $230 \lesssim L_s \lesssim 240^\circ$  after the functioning of the vents  $L_s \lesssim 220^\circ$ .

In the next phase, starting at  $L_s \approx 240^\circ$ , we observe a steady rise of seasonal AOD in association with an increasing day-to-day variability. Conjointly for

$244 \lesssim L_s \lesssim 248^\circ$  a transition between the “yellow” and “red” regimes occurs. That means that, thereafter, the AOD is statistically higher during the afternoon than during the morning and more so than during the early hours with low to moderate spread. Despite the growing activity of the second phase, the increase of seasonal AOD is late compared to unit 2. This is somewhat surprising since unit 1 is the sector for which the inner crocus line is progressing the fastest. Our interpretation relies on the fact that, with the wide separation between the inner and outer crocus lines, spatially segregated defrosting patterns cover a very extended area for the considered time period  $240 \lesssim L_s \lesssim 260^\circ$  ([Schmidt et al., 2009](#)). As a consequence during daytime, and at the  $\approx$  kilometre scales, local temperature contrasts are huge promoting powerful convection cells but of reduced size in the boundary layer with associated thermal gusts ([Spiga and Lewis, 2010](#); [Siili et al., 1999](#)). They become stronger with LT. Besides during nighttime, with reduced thermal contrasts and temperature inversions above high-standing icy surfaces, the katabatic wind regime could recover for a few hours. Conjunction of the two phenomena - katabatic winds (KW) more efficiently than small scale convection (SSC) - restrict atmospheric upward diffusion and dust accumulation above the region to some degree.

By  $L_S \approx 260^\circ$  the area corresponding to unit 1 is entirely defrosted. Higher in latitude the separation between the inner and outer crocus lines is shrinking. We have the emergence of a persistent regional AOD maximum that grows in value and spatial extent and reaches its height at  $L_S = 272\text{--}274^\circ$ . That corresponds to the maximum level of mean seasonal AOD for the unit which is then also the most spatially segregated in terms of  $\tau_{det}^{k0}$ . Unit 1 evolves from a red regime to a regime for which the night hours display significantly higher AOD than during daytime even though opacity’s stay persistently at high level in agreement with the transient event observations (Section 3.5). These elements drive the following interpretation for the third phase. The conjunction several mechanisms for atmospheric dust enhancement in the region could be envisioned. First the advection and upward diffusion (AD2) of dust from the retreating distant edge of the cap. As explained before preferentially katabatic ([Siili et al., 1999](#))

winds but also possibly cap edge winds (CW) both able to carry dust (Toigo et al., 2002) blow outward from area that are still in the second phase. In section 4.5, we discuss more thoroughly the occurrence and functioning of these daytime thermal mesoscale breezes. Second thermal gusts and dust devils associated to the standard convective activity (Spiga, 2011; Spiga and Lewis, 2010). Third synoptic circulation (SC) and especially low pressure systems can interfere with the latter mechanisms and explain the special persistence of regional AOD maxima's in the region.

The fourth and last phase corresponds to the decline of seasonal AOD after  $L_S \approx 270^\circ$  with the related diminishing day-to-day variability or, equivalently, spatial heterogeneity. At this point the crocus line is remote from the “cryptic” region and has stopped being a source of dust. Hence the thermal gusts and dust devils (DD) persist exclusively inducing moderately efficient dust lifting and upward transport.

#### 4.2. Unit 2

For unit 2 we distinguish three successive phases of activity.

The first one stretches from the beginning of the covered period to  $L_S \approx 235\text{--}240^\circ$  when the region is still entirely covered by the seasonal CO<sub>2</sub> deposits. From a starting value of  $\approx 0.5$  the mean AOD steadily grows regardless of the crocus date in many places which are spatially coherent in their behaviour. Therefore we suggest that the advection of dust at high altitude (AD1) from the lower active latitudes is the main origin of the increasing atmospheric opacity. Meteorological maps (not included here) of wind intensity and direction were extracted from GCM simulations (Forget et al., 1999) for the southern high latitudes ( $\geq 60^\circ\text{S}$ ) and examined. They show that poleward air fluxes at synoptic scales are well developed between 5 and 11 km at this season and nearly reach the pole. Such fluxes correspond to the return branch of a large scale convection cell that is established between the cold cap and the surrounding warming ice free terrains. Due to orographic differences or due to the different extension of the transition zone, this synoptic feature could be more strongly established

at the longitudes of unit 2 than at those of unit 1. Indeed the situation differ markedly between the two units during this early period.

During the second phase  $240 \lesssim L_s \lesssim 265^\circ$  the climb of seasonal AOD levels continues at the same overall rate while the crocus lines sweep the unit. The defrosting area that presents a geographical mixture of ice-free and still frozen terrains implying high thermal contrasts is more limited in extent than for unit 1, of the order of 2 to  $5^\circ$  in latitude. Day-to-day variability  $var_{D2D}$  is also progressively on the rise with a neat apogee in the defrosting area. Meanwhile several regional maxima's develop after the passage of the crocus line, and the peak of atmospheric opacity due to aerosol is reached at  $L_S \approx 265^\circ$ . We put forward the hypothesis that unit 2 shares common processes with unit 1, those prevailing during the second and third phases of the latter, with one crucial difference. Similarly to unit 1, we have in the defrosting area daytime dust lifting associated to small scale convection cells (SSC) with intense thermal gusts. This mechanism is triggered by the high thermal contrasts. Contrary to unit 1, where topography allows for nighttime katabatic winds, the only mechanism to blow efficiently dust downstream are the daytime thermal cap winds (CW) that are established at the mesoscales between the SSPC and the defrosted terrains (Toigo et al., 2002). Indeed they likely allow for vertical diffusion of dust in the atmosphere to some extend and transport (AD2) towards the lower latitudes that are entirely defrosted. The whole scheme is compatible with the occurrence of most transient dust events during the afternoon in this region.

In the third phase, when the outer crocus line definitively left unit 2,  $var_{D2D}$  declines soon followed by the seasonal level of AOD. Such a behaviour, equivalent to phase 4 of unit 1, has likely the same origin: non efficient dust lifting by gusts and dust devils (DD).

#### 4.3. Unit 3

This unit is characterised by a first phase of gradually enhanced dust opacity rather similar to the one experienced by unit 2 until  $L_S \approx 250^\circ$ . The difference resides in the fact that before  $L_S \approx 245^\circ$ , the atmospheric dust layer is more

uniform than anywhere else especially in the area of the “Mountain of Mitchell”. As a consequence, the day-to-day variability is also very low and no signs of local time dependencies (at least for the highest latitudes) can be noted. The advection of dust by the synoptic circulation (AD1) from active area at lower latitudes is probably the main origin for the increasing atmospheric opacity with no contribution of a local activity because all the unit is still frozen during this phase.

The situation starts to change after  $L_S \approx 250^\circ$  with the gradual sweeping by the crocus lines, the day-to-day variability that becomes significant, and the emergence of a “red” regime associated to moderate to low spread regarding the behaviour of AOD as a function of local time. In the defrosting area, a relative clearing of the atmosphere is observed especially since the inner and outer crocus lines are well separated ( $L_S \gtrsim 255^\circ$ ). The clearing sometimes spreads beyond the principal outer crocus line particularly for  $266 \lesssim L_s \lesssim 274^\circ$  in the area of the “Mountain of Mitchell” (then in their last phase of defrosting) and around Dorsa Argentera around  $L_S \approx 275^\circ$ . As for the cryptic region in its second phase, the geographical mixture of ice-free and still frozen terrains implies local high thermal contrasts in turn promoting intense but small scale convection cells (SSC). They are in phase with the diurnal cycle and provide enough surface stresses to raise the dust (Toigo et al., 2002). However this mechanism confines the dust to low altitudes where it is not efficiently detected by our method due to the poor radiative coupling with the gas. Also it somewhat moderates the evacuation of the dust downstream. Note that, unlike what goes on in unit 1 during phase 2, the katabatic winds cannot take over since no significant slopes can be found at the regional scale in the longitude sector of unit 3. Furthermore the mesoscale daytime thermal breezes could also be inhibited by the broad width of the transition zone, i.e. the absence of a sharp thermal boundary of regional proportions. The previous elements converge so as to limit dust opacity around the SSPC in unit 3 even though it gradually increases.

#### *4.4. Unit 4*

We think that this unit can be divided into two sub-units each one being characterised by specific mechanisms despite their very comparable but likely coincidental behaviour. Sub-unit 4a mainly corresponds to the lowest latitudes that we cover in the “anti-cryptic” sector whereas sub-unit 4b lies basically in the region of the south permanent polar cap (SPPC).

Sub-unit 4a very much behaves like unit 3 but in advance of seasonal phase. In the period  $220 \lesssim L_s \lesssim 240^\circ$  advection of dust from the lower latitudes is the preferred mechanism for explaining relatively high AOD levels. Around  $L_s \approx 250^\circ$  with the passage of the crocus line, a local minimum of seasonal AOD is reached due to the concentration of dust at low altitudes by the small scale convection cells of the relatively narrow transition zone. Thereafter a progressive and marked rise of dust opacity intervenes (from 0.55 to 0.8) that we attribute to the advection of dust by the mesoscale thermal cap winds blowing from the defrosting area that is moving away. Note that the equivalent relative clearing of the atmosphere observed higher in latitude (Unit 3) at the same time seems to be correlated in longitudinal position with the development of two regional maxima’s of dust opacity in Unit 4 centred at  $(70^\circ\text{S}, 320^\circ\text{E})$  and  $(65^\circ\text{S}, 30^\circ\text{E})$ . The latter persists for at least  $\approx$  twelve days, was spotted by several OMEGA observations and displays unusual hues in the visible. Then the thermal winds fade gradually to be replaced by thermal gusts and dust devils.

For sub-unit 4b the initial rise of seasonal AOD until  $L_s \approx 235^\circ$  and then decline down to  $\approx 0.5$  at  $L_s \approx 250^\circ$  shows no signs of local time dependencies nor appreciable low day-to-day variability. This conjunction of factors supports the hypothesis that dust opacity is then controlled by large scale dynamics transporting dust high in the polar atmosphere. By  $L_s \approx 250^\circ$  the atmosphere above the SPPC sees a strong and continuous enhancement of seasonal AOD. Meanwhile we observe an increasing then a decreasing day-to-day variability, the latter evolution being well correlated with the trends affecting the same indicator for the “cryptic” region. As far as the local time dependencies are concerned we are rather in a “red” regime with modest spread. On a broader

time scale amount of advected dust changes with time and may be characterised by episodes of transient yet important rises of opacity that span a large range of longitudes at  $L_S \approx 241$ , 254, and  $270^\circ$  as shown by the Hovmöller diagram of Figure 8 . Therefore we suggest that the SPPC undergoes the influence of units 1 and 2 activity by migration of dust clouds toward the pole at altitudes of a few kilometres thanks to the return flow of the thermal cap winds (Section 4.5). Influence of unit 3 and 4a might be more reduced due to the relative inhibition of the mesoscale thermal winds as evoked earlier.

#### *4.5. Comparison with earlier works*

In the previous sections we propose an interpretation regarding the aerosol activity of the southern polar region in which two mechanisms play a major role for lifting and transporting efficiently mineral particles and create dust events or storms: (i) nighttime katabatic winds at locations where a favourable combination of frozen terrains and topography exists (e.g. unit1) (ii) daytime mesoscale thermal winds at the edge of the cap when the transition zone is sufficiently narrow (e.g. unit2). Thermal gusts due to the high thermal contrasts associated to segregated terrains in the defrosting area could also pick up some dust but likely leads to limited vertical and horizontal transport (e.g. unit4a).

[Siili et al. \(1999\)](#) performed a set of numerical experiments with the two-dimensional Mars Mesoscale Circulation Model to study this kind of processes that control wind patterns and potentially dust lifting: sloping topography and thermal contrasts at the seasonal cap edge. In particular they demonstrate that strong near surface winds potentially capable of lifting dust from the surface can be achieved (i) in daytime along a slope which lower section is frozen and upper section is ice-free: “anabatic winds” (ii) in nighttime over a fully ice-covered slope or defrosted in its lower section: “katabatic” winds. Inclusion of atmospheric dust ( $\tau = 0.3$ ) reduces the daytime ice-edge forcing - the upslope flow is attenuated - while the nocturnal downslope flow is enhanced. These results inspired some of our interpretations and suggest additionally that small scale convection in the defrosting area can be linked with local relief. Note that

the latter also controls spatial segregation of frozen and ice free terrains through slope orientation for example.

Toigo et al. (2002) have studied the development of the cap winds, analogues to terrestrial sea breeze circulation generated by the strong thermal contrasts that exist along the retreating edge of the southern spring polar cap during the middle to late spring. Their three-dimensional numerical modelling at meso-scales demonstrate that surface wind stresses are sufficient at some location during specific local time intervals to initiate movement of sand-sized particles and hence dust lifting. Thus they recognise cap edge winds as an important factor for the development of dust storms near the cap edge. In addition the important dynamical modes generating high wind stresses are isolated, the direct cap-edge thermal contrast (and topographical slopes in some locations) providing the primary drive. However the influence of a having a gradual transition between the inner and outer crocus lines instead of a neat cap edge and the availability of dust and/or sand particles are not addressed in their paper. It should also be noticed that dust lifting mechanisms such as dust devils are not accounted for by their modelling. As regards to the details of the atmospheric dust spring activity, Toigo et al. (2002) perform three simulations ( $L_S = 225$ ,  $255$ , and  $310^\circ$ ) with the Mars Mesoscale Model MM5 run with time-evolving conditions provided at the simulation domain boundary by the GFDL Mars GCM. In the south polar region (latitudes higher than  $50^\circ\text{S}$ ) surface wind stresses are calculated and aerosol optical depth is derived based on a simple dust injection scheme. The simulations exhibit a great deal of time variability that is mostly related to variations in local time, the day-to-day variations in location and extent of the area of high surface wind stresses being negligible. This property is confirmed by our results since they show that the highest variability around the mean trend is achieved at the locations experiencing cap winds and downstream because of associated dust advection. At  $L_S = 225^\circ$  a great deal of lifting along the cap edge occurs at all longitudes, especially between noon and 18:00 LT. Significant activity is also visible at some places during night and morning. As a result, wisps of dust trail away from many locations and filamentary dust

clouds from previous injection events abound within the simulation domain. That corresponds to the situation depicted by their TES map at  $L_s \approx 227.5^\circ$  in which infrared opacity can be in excess of 0.5 all around the edge of the polar cap while it remains between 0.1 and 0.2 at lower latitudes (background level). Our AOD maps generated from individual observations taken by OMEGA at the beginning of the period of interest ( $220 \lesssim L_s \lesssim 242^\circ$ ) cover large strips of Mars, joining across the cap areas of opposite longitudes at moderate latitudes (Section 3.5). The regions external to the cap (latitudes below  $\approx 70^\circ S$  that are not visible in our mean trend mosaics, Fig.12) indeed display extended cloud systems following  $L_s \approx 225^\circ$  for varied longitude sectors, regardless of local time. In the simulation of [Toigo et al. \(2002\)](#), some amount of the injected dust is blown over the seasonal ice cap in agreement to what we observe in the “afternoon” side. Such a situation can be explained by the high altitude return flows of the mesoscale cap winds. At  $L_s = 255^\circ$ , according to the simulation of [Toigo et al. \(2002\)](#), noticeable lifting is now concentrated at the immediate cap edge between  $270$ - $60^\circ E$  for LT in the range 07:00-22:00. The maximal extent occurs during the early afternoon. Dust are thus advected daily towards lower latitudes resulting typically in two concentric filaments, one close to the cap edge, the other northward. Decay of the cloud back to background levels of optical depth takes about one day. Additional lifting occur on the SPLD centred at  $180^\circ E$  between 19:00 LT and midnight while Chasma Australis shows signs of activity in predawn morning. In the latter case, nighttime drainage flow off the seasonal cap (katabatic winds) is invoked. However this latest mechanism does not lead to important dust clouds. In the TES map at  $L_s \approx 257.5^\circ$  significant accumulation of dust is restricted to the longitudes from  $270$  to  $45^\circ E$  in broad agreement with the simulation. At contrary the most productive area in our case around  $L_s \approx 255$ - $260^\circ$  of MY 27 is in the longitude sector  $180$ - $300^\circ E$  (unit 2), rather in agreement with the results of [Imamura and Ito \(2011\)](#) (see below). Nevertheless, for the cryptic sector, we adhere to the idea of late hour katabatic winds enabled by topography and lifting dust while suggesting an additional role: inhibiting dust vertical migration. Filamentary and transient dust clouds

propagating from the cap edge to the lower latitudes are predicted by [Toigo et al. \(2002\)](#) from their simulations but do not show up in our Hovmöller diagrams (Figures 9 and 8). The limited time resolution of the OMEGA observations may constitute an explanation. In midsummer ( $L_s = 310^\circ$ ) in the simulation of [Toigo et al. \(2002\)](#) typical dust activity near the south polar cap is much decreased in general, and the appearance of dust clouds is both smaller and much less frequent. Since our monitoring stops at  $L_s = 280^\circ$  we cannot make a direct comparison but the declining mean trend we note for all units after  $L_s \approx 270^\circ$  is compatible. The general decrease of AOD after  $L_s \approx 265\text{--}272^\circ$  depending on the unit is linked with the fading of the influence of the thermal cap winds  $\approx 10^\circ$  solar longitude after the passage of the outer crocus line.

For Martian Year (MY) 24,  $L_s=270\text{--}280^\circ$ , the TES map by [Imamura and Ito \(2011\)](#) displays an elongated dusty region that encircles the south pole with a gap in the range  $330\text{--}60^\circ\text{E}$ ; this feature was also observed in MY 25 and 26. The map is part of a larger study that also addresses the temporal and spatial variation of the  $9\text{ }\mu\text{m}$  dust optical depth in this region using Hovmöller diagrams for three Martian years. For the range of solar longitudes  $240 \lesssim L_s \lesssim 300$ , [Imamura and Ito \(2011\)](#) found that dust clouds emerge repeatedly (every 10–20 sols) from an area delimited by latitudes  $70\text{--}80^\circ\text{S}$  and longitudes  $240\text{--}300^\circ\text{E}$ . Then they move westward and reach the region in the longitude sector  $60\text{--}120^\circ\text{E}$  to finally disappear. The overall longitude range of the disturbance,  $60\text{--}300^\circ\text{E}$ , coincides with elevated terrains in the south polar region, and with the increase of dust optical depth observed at  $L_s=270\text{--}280^\circ$  that encircles the south pole. Based on the previous observations [Imamura and Ito \(2011\)](#) draw the conclusion that the mechanism of dust lifting around the south seasonal cap is not as clear as proposed by [Toigo et al. \(2002\)](#). Following [Siili et al. \(1999\)](#), they claim that the periodic nature of the dust cloud generation could be linked to suspended dust near the cap. Indeed the latter reduces the temperature contrast via absorption of sunlight, subsequently diminishing surface stress if it is distributed over both the frozen and ice-free terrains. In this case, there could be a negative feedback between dust loading and temperature contrast, leading to the quasi-periodic

behaviour (period of 10–20 sols) of the dust optical depth disturbance that is recognised in the latitude band 70–80°S by [Imamura and Ito \(2011\)](#) in their Hovmöller diagrams. On the other hand it can be noted that, in the main source regions where prevail cap winds (Unit 2 then Unit 1), the modulation is absent from our curves of seasonal AOD. This suggests that the possible negative feedback between dust loading and atmospheric temperature contrast across the cap edge was not operating at least for MY27.

These facts can be clarified by assuming that the cap edge thermal contrast generates in theory a circulation cell comprised of a outward flow over the ice cap (i), a near-surface off-cap horizontal flow (ii), a upward flow above the ice-free regolith (iii), and a weaker return flow higher up (iv) ([Siili et al., 1999](#)). Zone (ii) is the principal source but the dust is revealed to us when undergoing vertical migration in zone (iii) up to the cell height (of the order of few km). Another consequence of this scheme is that, above the cap, dust is mostly confined to high altitudes because advection from lower latitudes is the only provider, the surface still being entirely frozen. Consequently the thermal profile of the first hundred meters is not affected by dust and the lowest atmospheric layers above the ice remain very cold. The vigorous convection occurring in the defrosting area at smaller scales may alter this large pattern. For unit 2 in particular dust seems to be raised sufficiently high so as to become visible to us in zone (ii). However details of the interaction between the two mechanisms are not accessible by our results. Finally we also saw the sign of a mostly meridional return flow over the SPPC starting at  $L_S \approx 250^\circ$  that leads to a continuous increase of the AOD over the south pole at least until  $L_S \approx 270^\circ$ .

## 5. Summary

The OMEGA instrument has acquired a comprehensive set of observations in the near-infrared (0.93–5.1 microns) at the high southern latitudes of Mars from mid-winter solstice ( $L_S = 110^\circ$ , December 2004, MY 27) to the end of the recession ( $L_S = 320^\circ$ , November 2005). We systematically process a subset of these observations from  $L_S = 220^\circ$  to  $280^\circ$  by performing the inversion of a radiative

transfer scheme described in a companion paper on every top of the atmosphere reflectance spectra forming the OMEGA images. As a result, we obtained a series of maps depicting the distribution of aerosol optical depth (AOD) noted  $\tau_{aer}^{k0}$ . The maps were de-trended in order to correct for changes due solely to varying atmospheric height because of topography. They were independently integrated into a common grid generated from the Hierarchical Equal Area isoLatitude Pixelization of Mars southern hemisphere. Such an integration, that can be performed at different spatial resolutions, allows to build the time evolution of the AOD for each spatial bin of the Healpix partition. We then separate two contributions: a mean trend of  $\tau_{det}^{k0}$  versus time, i.e. the baseline, and a highly variable component, i.e. the day-to-day variability around the baseline with an adapted method. We also implement a data processing to isolate any dependencies to the local time (diurnal cycle) of a given bin. The HEALPIX system provides means to map the values of atmospheric opacity or of any derived quantity for a certain date or averaged over a time interval according to different geographical systems. Thus we generate time series of orthographic mosaics depicting spatio-temporal distribution of the seasonal mean values, the variance and the local time dependence of the AOD. Besides, although the modelling of the seasonal trend is performed in a pixel-wise manner, the spatial coherency of the mosaics is excellent. Then we may expect that seasonal baselines can be gathered, based on similar shapes, into a limited number of classes. This was confirmed by performing a kmeans classification that gives four main types of seasonal trends followed by the AOD  $\tau_{det}^{k0}$  in four units segmenting the southern polar region. Following this complete analysis of the data , each spatio-temporal unit was studied carefully for searching trends of atmospheric dust opacity.

As a result a synthetic view (Figure 15) of dust activity in the south polar atmosphere in mid spring to early summer has been established. From this compilation of observations we propose an interpretation of the behaviour of the four spatio-temporal units. Different mechanisms are involved at a variety of spatial scales and regarding the regression stage reached by the seasonal deposits. Based on our results we propose that two mechanisms play a major

role for lifting and transporting efficiently mineral particles and create dust events or storms: (i) nighttime katabatic winds at locations where a favourable combination of frozen terrains and topography exists (e.g. unit1,  $220^\circ \lesssim L_s \lesssim 255^\circ$ ) (ii) daytime mesoscale thermal winds at the edge of the cap when the defrosting area (transition zone) is sufficiently narrow (e.g. unit2,  $240^\circ \lesssim L_s \lesssim 260^\circ$ ). Indeed this kind of breezes could be inhibited, should the width of the transition zone be broad, i.e. in the absence of a sharp thermal boundary of regional proportions (e.g. unit4a,  $L_s \gtrsim 260^\circ$ ). Thermal gusts due to the high thermal contrasts associated to segregated terrains in the transition zone exist and could also pick up some dust but likely leads to limited vertical and horizontal transport (e.g. unit3,  $250^\circ \lesssim L_s \lesssim 270^\circ$ ). Far from the seasonal cap, gusts and vortexes associated with the convection of the boundary layer over ice-free terrains is not an efficient mechanism to inject large amount of dust in the atmosphere explaining the clear decline of the AOD after  $L_S \approx 270^\circ$  for the whole south polar region. Inside the seasonal cap, advection of dust at high altitude from the lower active latitudes is the main origin of the increase of the seasonal atmospheric opacity around  $L_S \approx 235^\circ$ , then  $L_S \approx 275^\circ$ . Such fluxes correspond to the return branch of a synoptic convection cell that is established between the cold cap and the surrounding warming ice free terrains. Due to orographic differences or due to the different extension of the transition zone, this synoptic feature could be more strongly established at the longitudes of unit 2 than at those of unit 1. In addition our Hovmöller diagrams reveal that advection of dust is not regular but undergoes pulses of increased or decreased intensity. We suggest that this modulation could result from the interaction of the convection cell with the baroclinic waves.

As regards to the production of atmospheric dust in the defrosting area, the most productive sector spans longitudes 180-300°E (unit 2) around  $L_S \approx 250^\circ$ . Later ( $L_S \approx 267^\circ$ ) the situation has changed drastically and the cryptic sector becomes the most productive while the longitude sector 300-60°E (unit 4a and 3) remain moderately dust-generative.

Our work thus contributes to understanding the sequence of phenomena

that control dust activity in the south polar atmosphere and suggests complex interaction between them. It calls for new simulations of the martian surface-atmosphere dynamics at mesoscales (between 1000 km and 1 km) considering topographical effects to reproduce the observations and to confirm the interpretations. In particular taking into account the gradual defrosting between the inner and outer crocus lines instead of considering a neat cap edge is of primordial importance. The local and regional availability of dust and/or sand particles needs to be addressed as well. Finally the possible interference of the baroclinic wave system with the convection cell that is established between the cold cap and the surrounding warming ice free terrains - including low altitude cap winds and high altitude return flows - must also been modelled properly.

### Acknowledgements

We thank the OMEGA team at Institut d’Astrophysique Spatiale for support with sequencing and data downlink activities. This work is supported by a contract with CNES through its Groupe Système Solaire Program. We are grateful to X. Ceamanos and A. Spiga for their reading of the manuscript and for fruitful discussions.

### References

- Basu, S., Richardson, M.I., Wilson, R.J., nov 2004. Simulation of the Martian dust cycle with the GFDL Mars GCM. *Journal of Geophysical Research (Planets)* 109 (E18), 11006–+.
- Chang, C.-C., Lin, C.-J., 2011. LIBSVM: A library for support vector machines. *ACM Transactions on Intelligent Systems and Technology* 2, 27:1–27:27, software available at <http://www.csie.ntu.edu.tw/~cjlin/libsvm>.
- Forget, F., Hourdin, F., Fournier, R., Hourdin, and Talagrand, C., O., Collins, M., Lewis, R., S., Read, and Huot, P. L., J., oct 1999. Improved general circulation models of the Martian atmosphere from the surface to above 80 km. *J. Geophys. Res.* 104 (13), 24155–24176.
- Górski, K. M., Hivon, E., Banday, A. J., Wandelt, B. D., Hansen, F. K., Reinecke, M., Bartelmann, M., Apr. 2005. HEALPix: A Framework for High-Resolution Discretization and Fast Analysis of Data Distributed on the Sphere. *ApJ* 622, 759–771.

- Imamura, T., Ito, Y., 2011. Quasi-periodic dust events in the summertime south polar region of mars. *Icarus* 211 (1), 498 – 503.  
URL <http://www.sciencedirect.com/science/article/pii/S0019103510003209>
- James, B., P., Cantor, A., B., Malin, andEdgett, M. C., andCarr, K., H., M., Danielson, E., G., Ingersoll, P.andDavies, A., E., M., Hartmann, K., W., McEwen, S.andSoderblom, A., A., L., Thomas, C., P., Veverka, J., apr 2000. The 1997 Spring Regression of the Martian South Polar Cap:Mars Orbiter Camera Observations. *Icarus* 144, 410–418.
- Kahre, M. A., Murphy, J. R., Haberle, R. M., Jun. 2006. Modeling the Martian dust cycle and surface dust reservoirs with the NASA Ames general circulation model. *Journal of Geophysical Research (Planets)* 111, 6008.
- Kauhanen, J., Siili, T., Järvenoja, S., Savijärvi, H., Sep. 2008. The Mars limited area model and simulations of atmospheric circulations for the Phoenix landing area and season of operation. *Journal of Geophysical Research (Planets)* 113, 0.
- Kieffer, H. H., Christensen, P. R., Titus, T. N., Aug. 2006. Co<sub>2</sub> jets formed by sublimation beneath translucent slab ice in mars' seasonal south polar ice cap. *Nature* 442 (7104), 793–796.  
URL <http://dx.doi.org/10.1038/nature04945>
- Kieffer, H. H., Titus, T. N., Mullins, K. F., Christensen, P. R., 2000. Mars south polar spring and summer behavior observed by TES: Seasonal cap evolution controlled by frost grain size. *J. Geophys. Res.* 105 (E4), 9653 – 9700.
- Langevin, Y., Bibring, J.-P., Montmessin, F., Forget, F., Vincendon, M., Douté, S., Poulet, F., Gondet, B., Jul. 2007. Observations of the south seasonal cap of mars during recession in 2004-2006 by the omega visible/near-infrared imaging spectrometer on board mars express. *J. Geophys. Res.* 112, –.
- Langevin, Y., Doute, S., Vincendon, M., Poulet, F., Bibring, J.-P., Gondet, B., Schmitt, B., Forget, F., Aug. 2006. No signature of clear co<sub>2</sub> ice from the /‘cryptic/’ regions in mars' south seasonal polar cap. *Nature* 442 (7104), 790–792.  
URL <http://dx.doi.org/10.1038/nature05012>
- Schmidt, F., Douté, S., Schmitt, B., Vincendon, M., Bibring, J.-P., Langevin, Y., The OMEGA Team, Apr. 2009. Albedo control of seasonal South Polar cap recession on Mars. *Icarus* 200, 374–394.
- Siili, T., Haberle, R. M., Murphy, J. R., Savijärvi, H., 1999. Modelling of the combined late-winter ice cap edge and slope winds in mars hellas and argyre regions. *Planetary and Space Science* 47 (8-9), 951 – 970.  
URL <http://www.sciencedirect.com/science/article/pii/S0032063399000161>
- Spiga, A., Aug. 2011. Elements of comparison between Martian and terrestrial meso-scale meteorological phenomena: Katabatic winds and boundary layer convection. *Planet. Space Sci.* 59, 915–922.
- Spiga, A., Lewis, S. R., 2010. Martian mesoscale and microscale wind variability of relevance for dust lifting. *International Journal of Mars Science and Exploration* 5, 146–158.

- Sugar, C., James, G., 2003. Finding the number of clusters in a dataset. *Journal of the American Statistical Association* 98 (463), 750–763.  
URL <http://www.tandfonline.com/doi/abs/10.1198/016214503000000666>
- Toigo, A. D., Richardson, M. I., Wilson, R. J., Wang, H., Ingersoll, A. P., Jul. 2002. A first look at dust lifting and dust storms near the south pole of Mars with a mesoscale model. *Journal of Geophysical Research (Planets)* 107, 4–1.
- Vapnik, V., 1998. *Statistical Learning Theory*. Wiley, New York.
- Vincendon, M., Langevin, Y., Poulet, F., Bibring, J.-P., Gondet, B., Jouglet, D., OMEGA Team, Aug. 2008. Dust aerosols above the south polar cap of Mars as seen by OMEGA. *Icarus* 196, 488–505.
- Wolff, M. J., Smith, M. D., Clancy, R. T., Arvidson, R., Kahre, M., Seelos, F., Murchie, S., Savijärvi, H., Jun. 2009. Wavelength dependence of dust aerosol single scattering albedo as observed by the Compact Reconnaissance Imaging Spectrometer. *Journal of Geophysical Research (Planets)* 114, 0–+.

Mean time interval of revisit (sol)

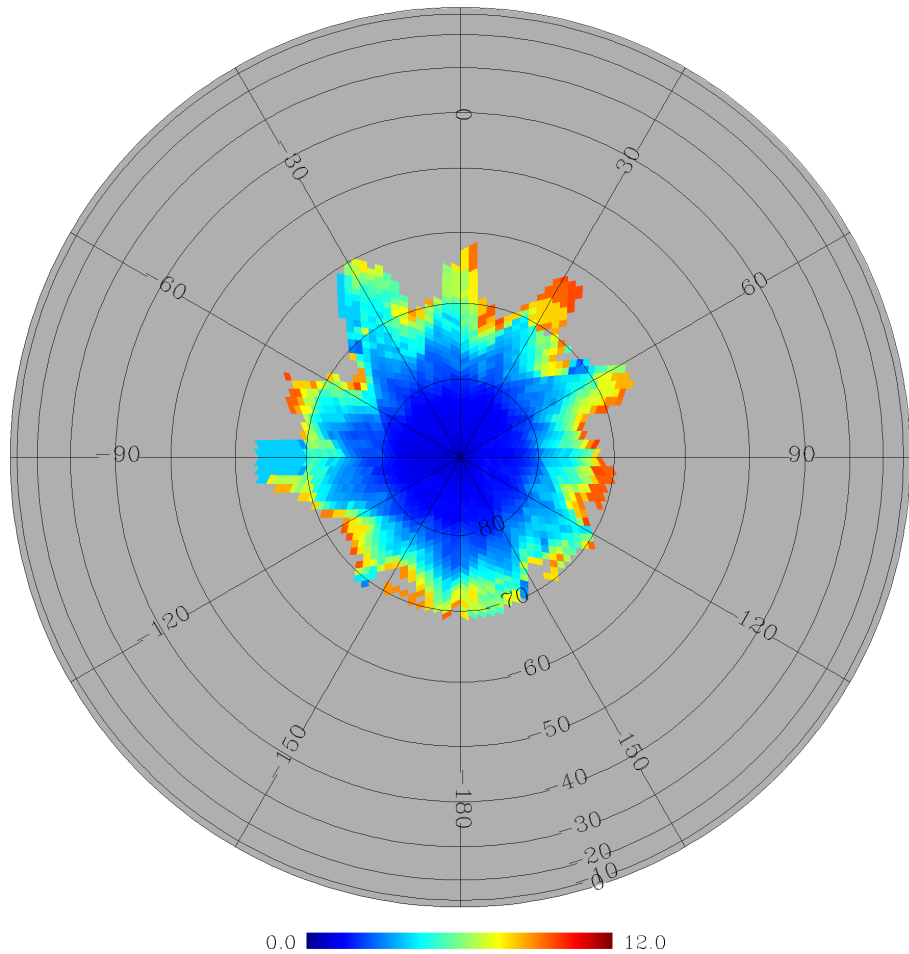


Figure 1: Mean period (in sols) of aerosol optical depth sampling for a given bin by the time series of OMEGA observations integrated into a common geographical Healpix grid of resolution  $1.0^\circ \cdot \text{pixel}^{-1}$ .

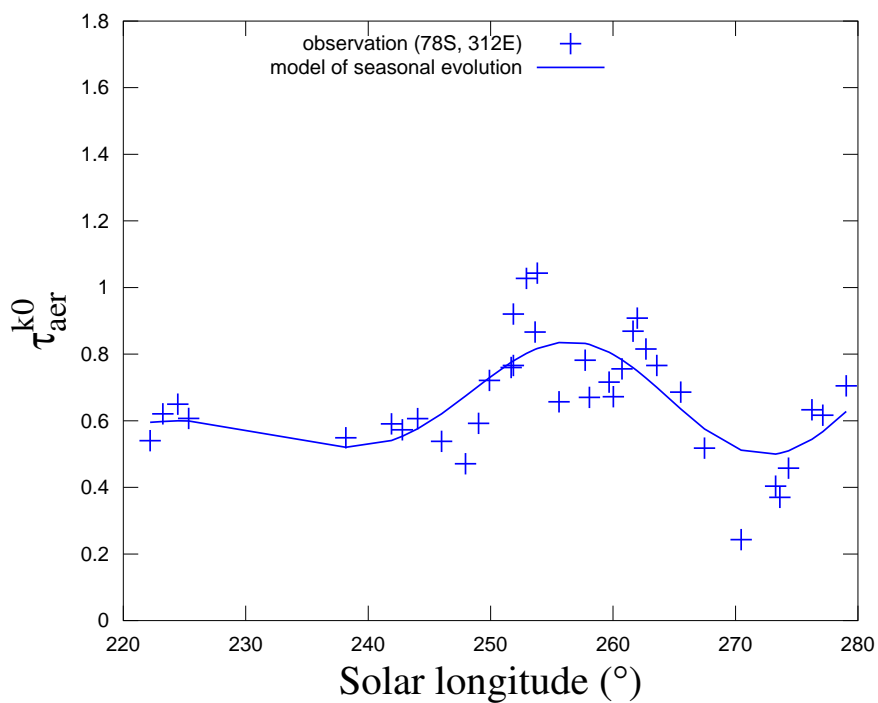


Figure 2: Time evolution of the AOD for a given bin of the PIDA (crosses) and modelling of its baseline by  $\epsilon$ -SVR (plain line).

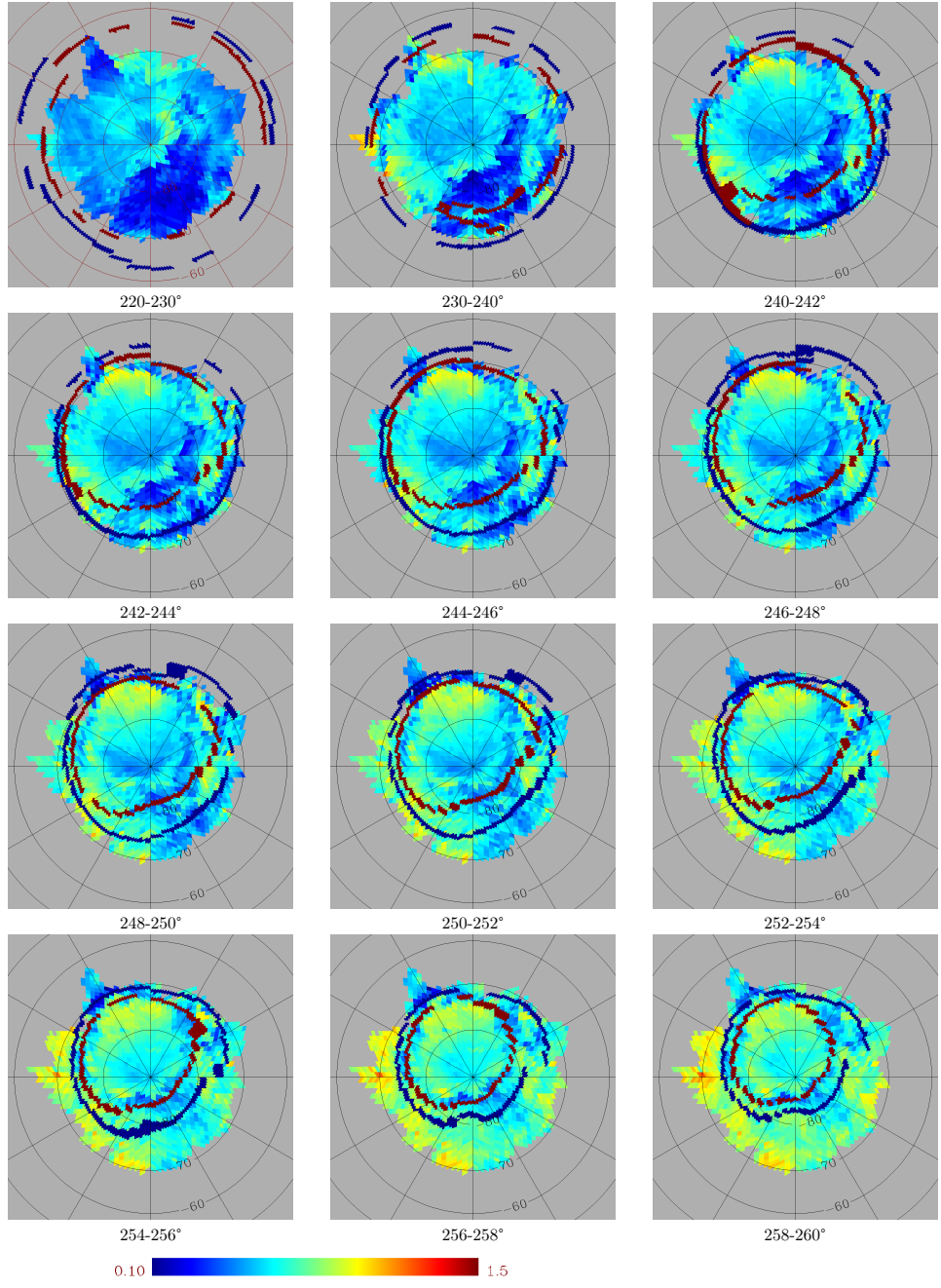


Figure 3: Time series of orthographic mosaics depicting from  $L_S=220^\circ$  to  $L_S=260^\circ$  the spatial distribution of seasonal mean values for the aerosol optical depth at 1  $\mu\text{m}$ . The inner (respectively outer) crocus line of the South Seasonal Polar Cap is coloured in red (respectively in blue).

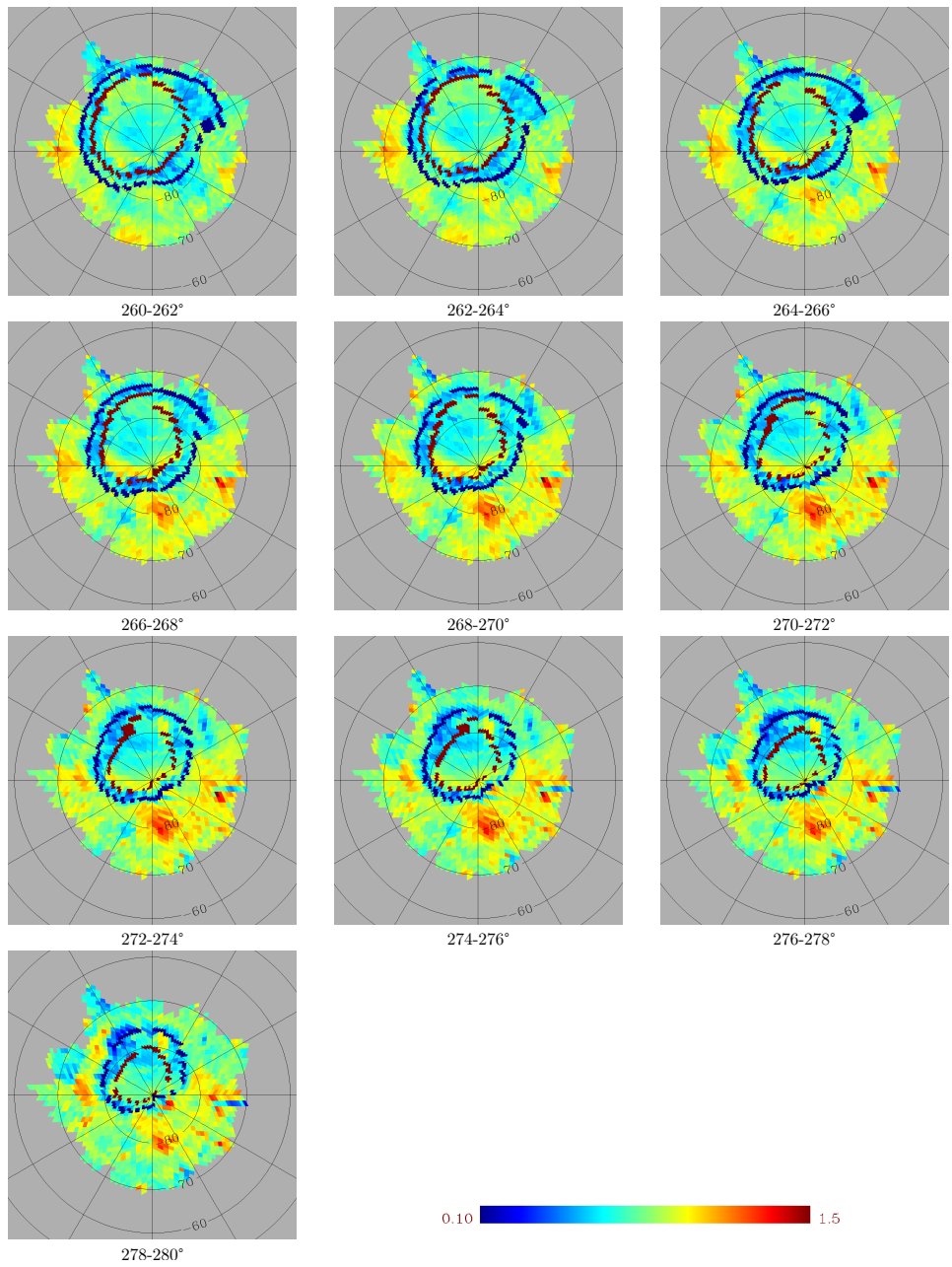


Figure 4: Same as in Figure 3 but from  $L_S=260^\circ$  to  $L_S=280^\circ$ .

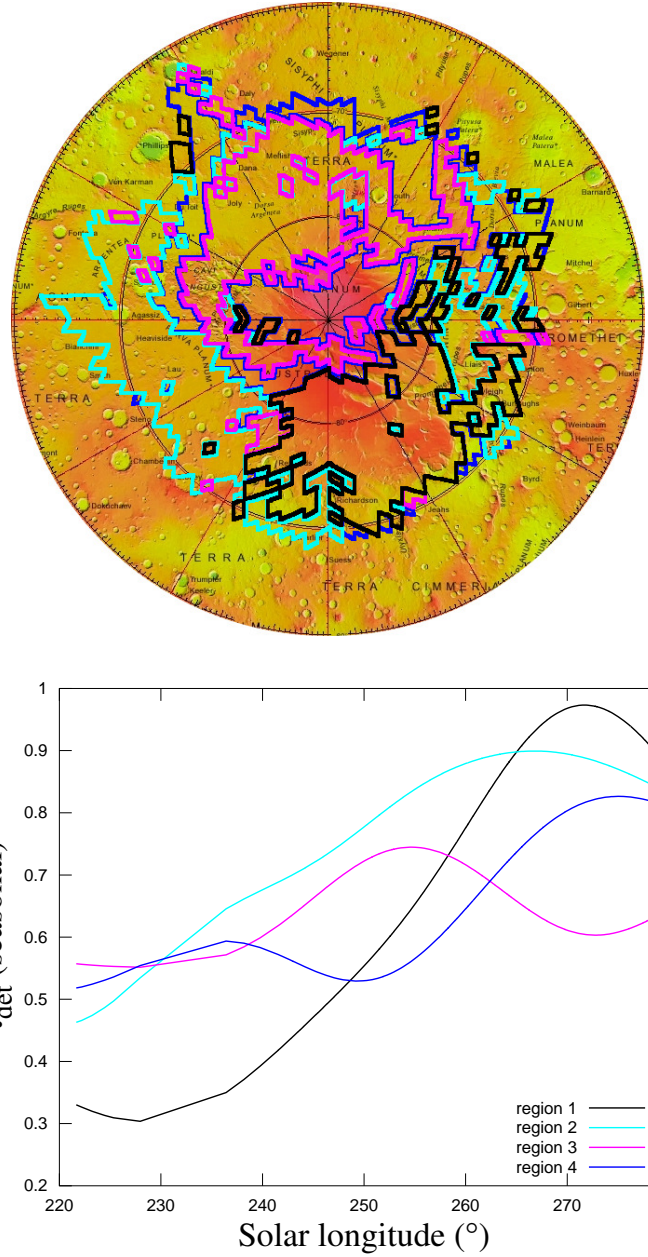


Figure 5: Characteristics of the four main classes of seasonal trends followed by the AOD  $\tau_{det}^{k0}$  in the southern polar region. (up) approximate spatial boundaries circling the area of most likely occurrence (down) corresponding seasonal baseline. See Section 3 for a detailed description.

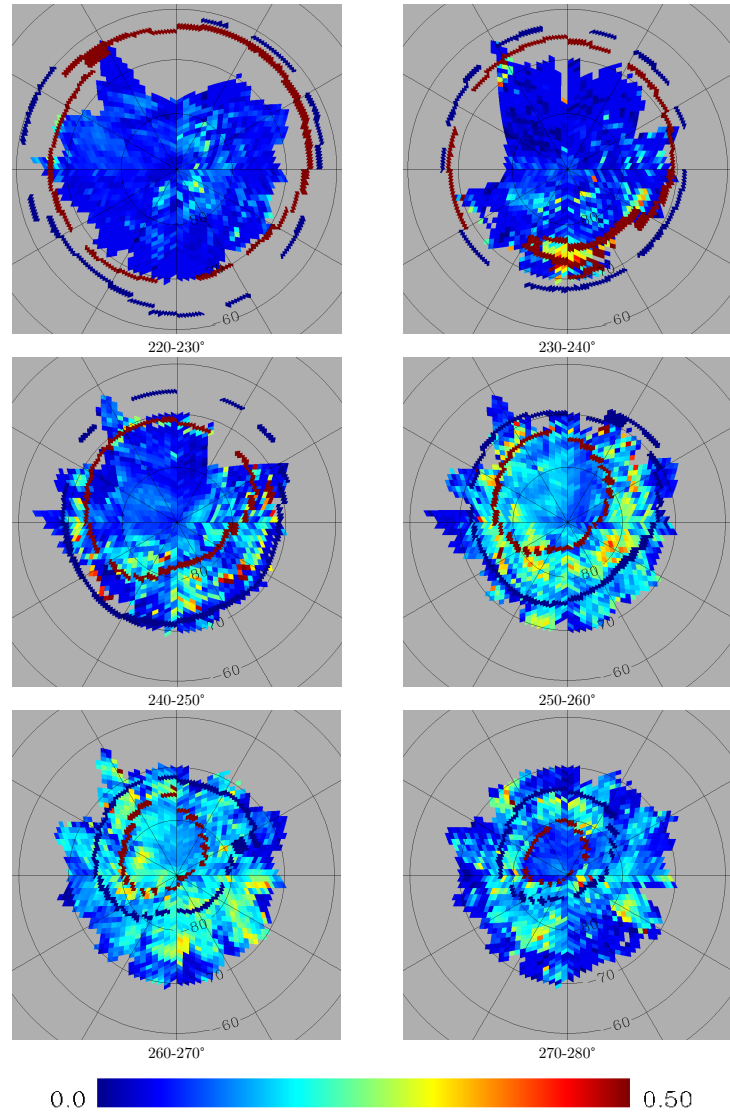


Figure 6: Time series of orthographic mosaics depicting from  $L_s=220^\circ$  to  $L_s=280^\circ$  the spatial distribution of day-to-day variance values for the aerosol optical depth at 1  $\mu\text{m}$ . The inner (respectively outer) crocus line of the SSPC is coloured in red (respectively in blue).

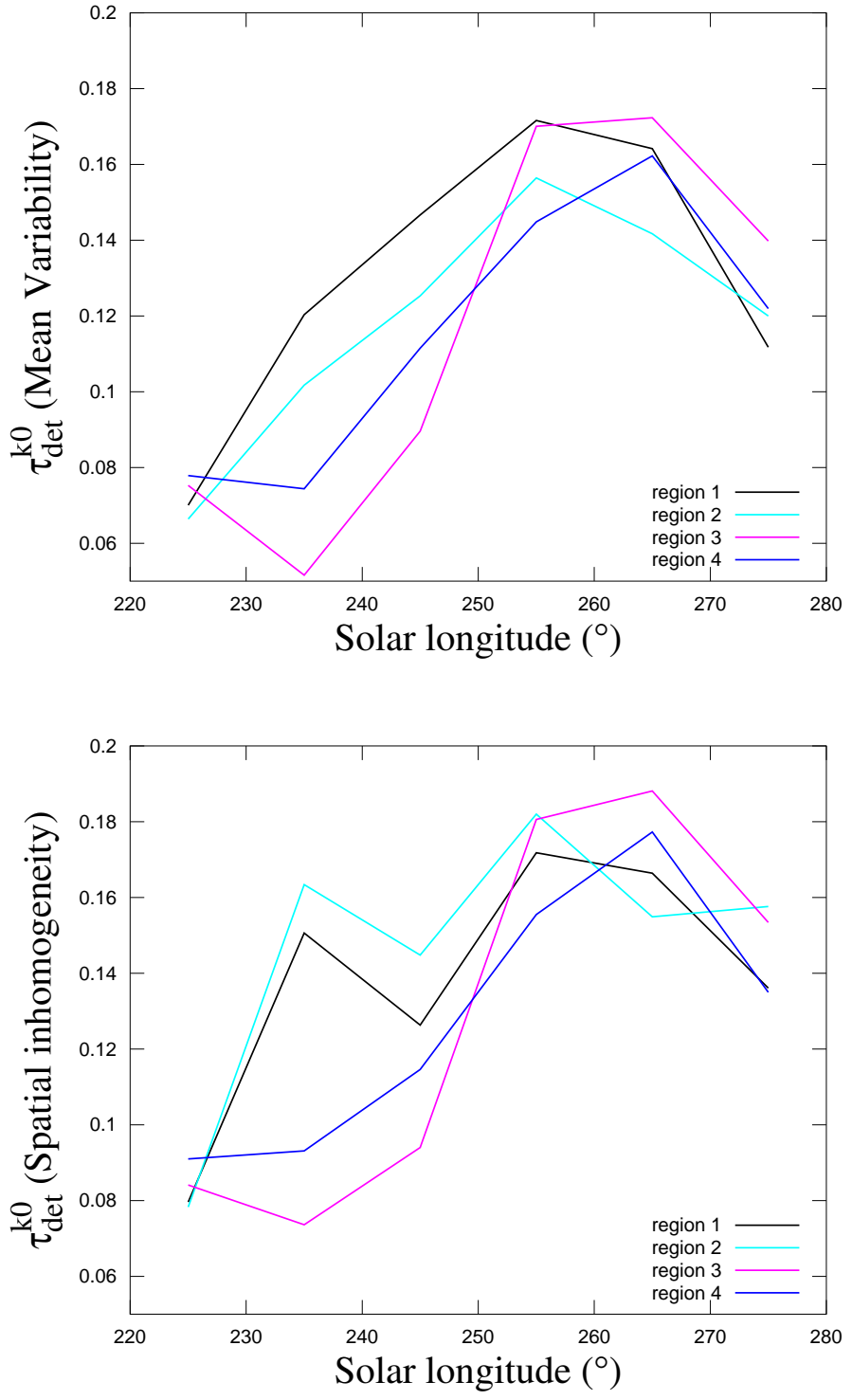


Figure 7: For each of the four spatio-temporal units, the average seasonal evolution of the day-to-day variability (up) and the seasonal evolution of spatial heterogeneity (down).

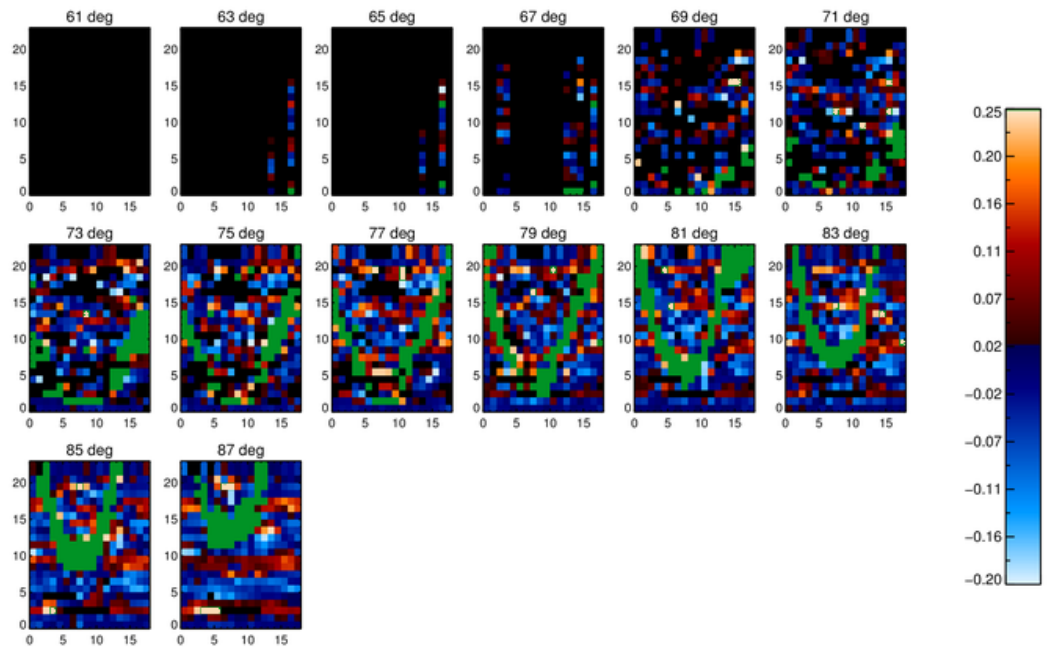


Figure 8: Hovmöller diagrams of the dust optical depth for fourteen latitude bands in the southern hemisphere during  $L_S = 220\text{--}280^\circ$  of Martian year 27. The central latitude of each  $2^\circ$ -width band is indicated at the top of each panel. The horizontal axis corresponds to longitudes (18 bins from 0 to  $360^\circ$ E), while the vertical axis corresponds to solar longitudes (24 bins). Black cells indicate lack of data while green cells pinpoint the position of the inner crocus line.

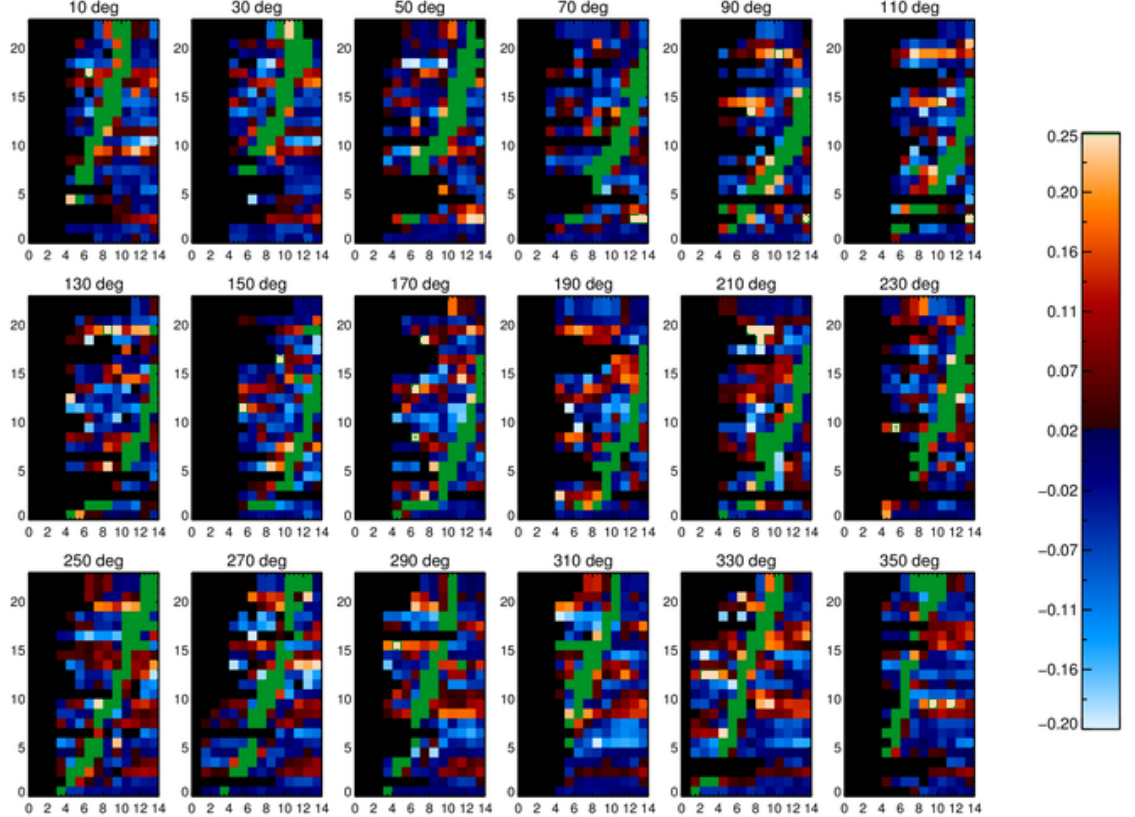


Figure 9: Hovmöller diagrams of the dust optical depth for eighteen longitude bands in the southern hemisphere during  $L_S = 220\text{--}280^\circ$  of Martian year 27. The central longitude of each  $20^\circ$ -width band is indicated at the top of each panel. The horizontal axis corresponds to latitudes (14 bins from 60 to 90S), while the vertical axis corresponds to solar longitudes (24 bins). Black cells indicate lack of data while green cells pinpoint the position of the inner crocus line.

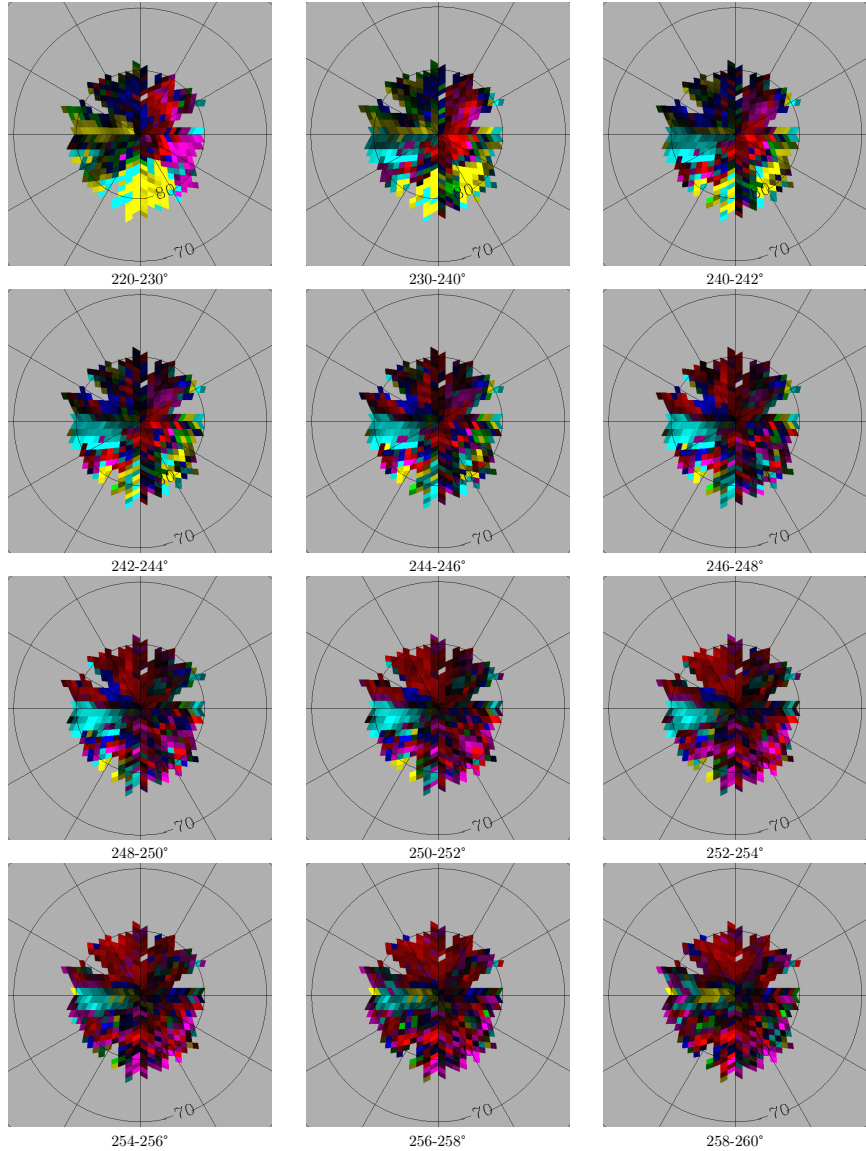


Figure 10: Time series of orthographic mosaics depicting from  $L_S=220^\circ$  to  $L_S=260^\circ$  the spatial distribution of local time dependency for the aerosol optical depth at  $1 \mu\text{m}$ . We assign to each bin a distinctive primary hue and a luminosity depending on the ordering of the triplet of LT  $\tau_{det}^{k0}$  values and on its variance  $var_{LT}$  as follows : 1: red  $B_{0-6} < B_{6-12} < B_{12-18}$ , 2: magenta  $B_{6-12} < B_{0-6} < B_{12-18}$ , 3: blue  $B_{0-6} < B_{12-18} < B_{6-12}$ , 4: cyan  $B_{6-12} < B_{12-18} < B_{0-6}$ , 5: green  $B_{12-18} < B_{0-6} < B_{6-12}$ , 6: yellow  $B_{12-18} < B_{6-12} < B_{0-6}$ . Colour bar appears in Fig. 11.

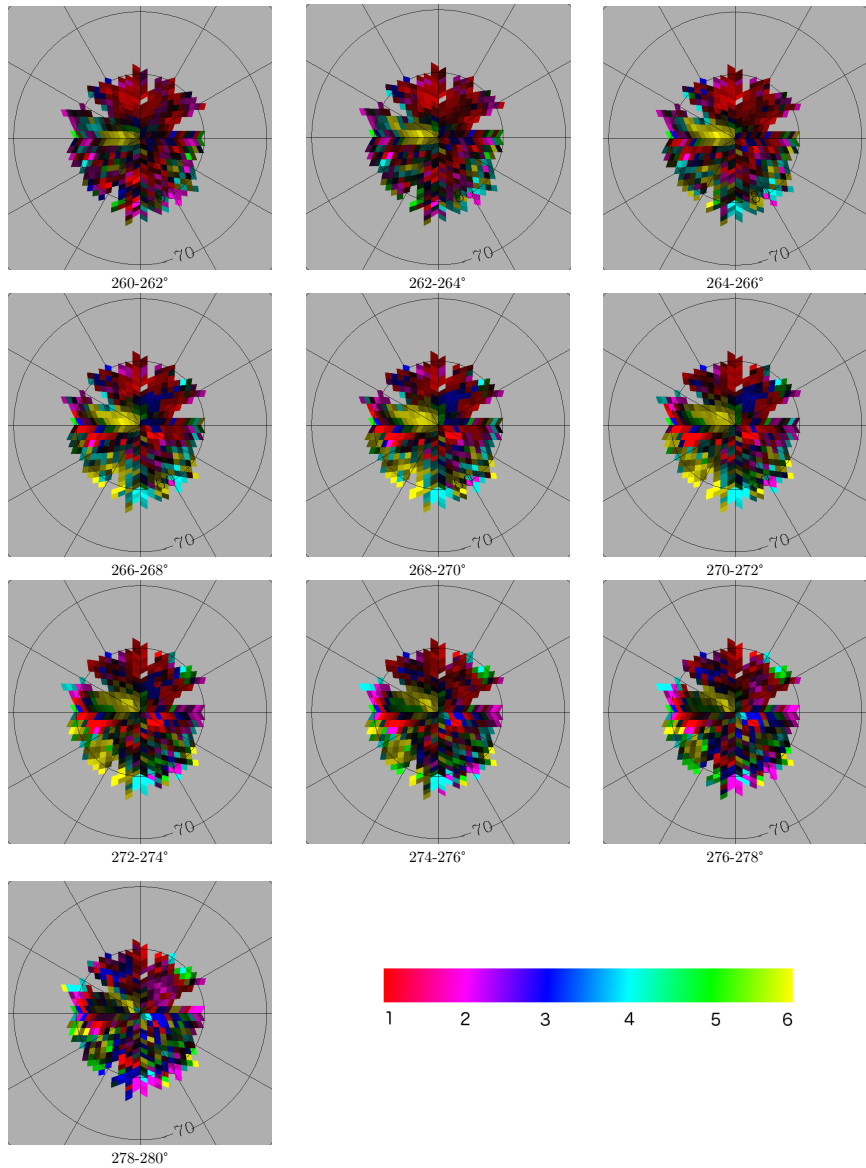


Figure 11: Same as in Figure 10 but from  $L_S=260^\circ$  to  $L_S=280^\circ$ .

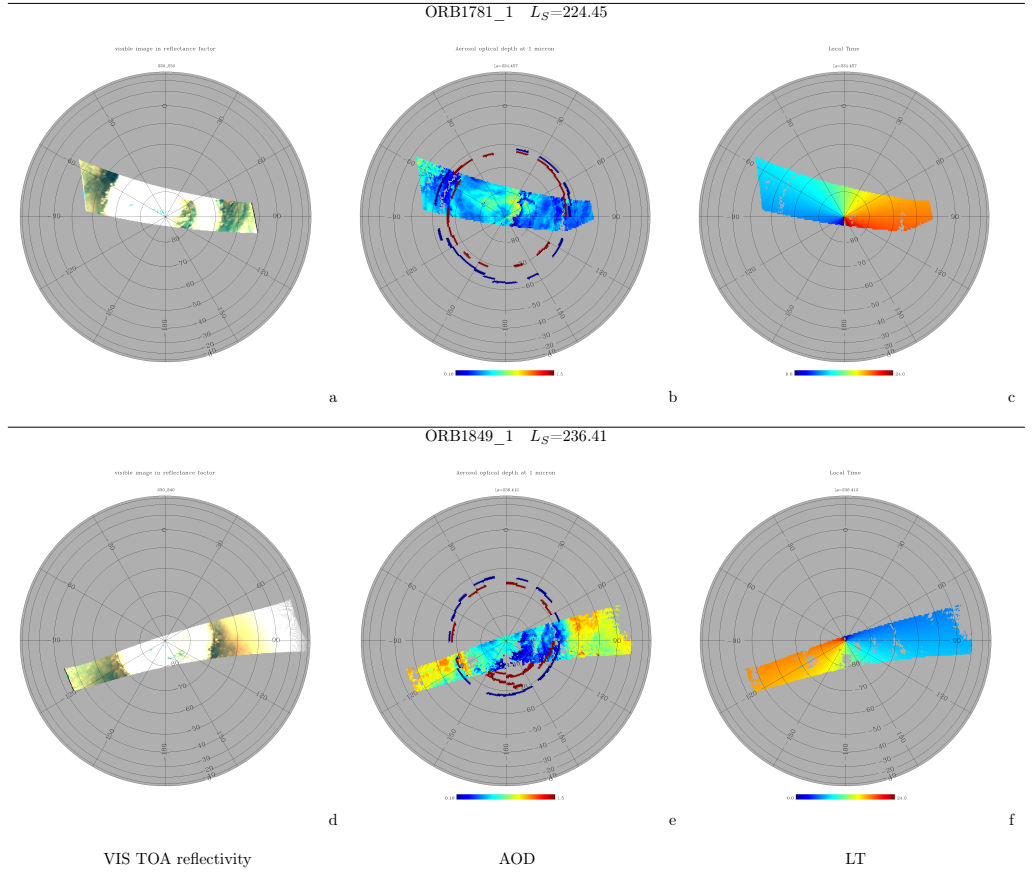


Figure 12: A selection of two global OMEGA observations and associated products. The left column displays an RGB composition of the TOA martian reflectivity in the visible which is stretched so as to reveal dust in the atmosphere as yellowish hues. The central column displays the Aerosol Optical Depth map at 1 micron. The right column displays a map which colour scale is used to indicate the local time of pixel acquisition. See the text for details.

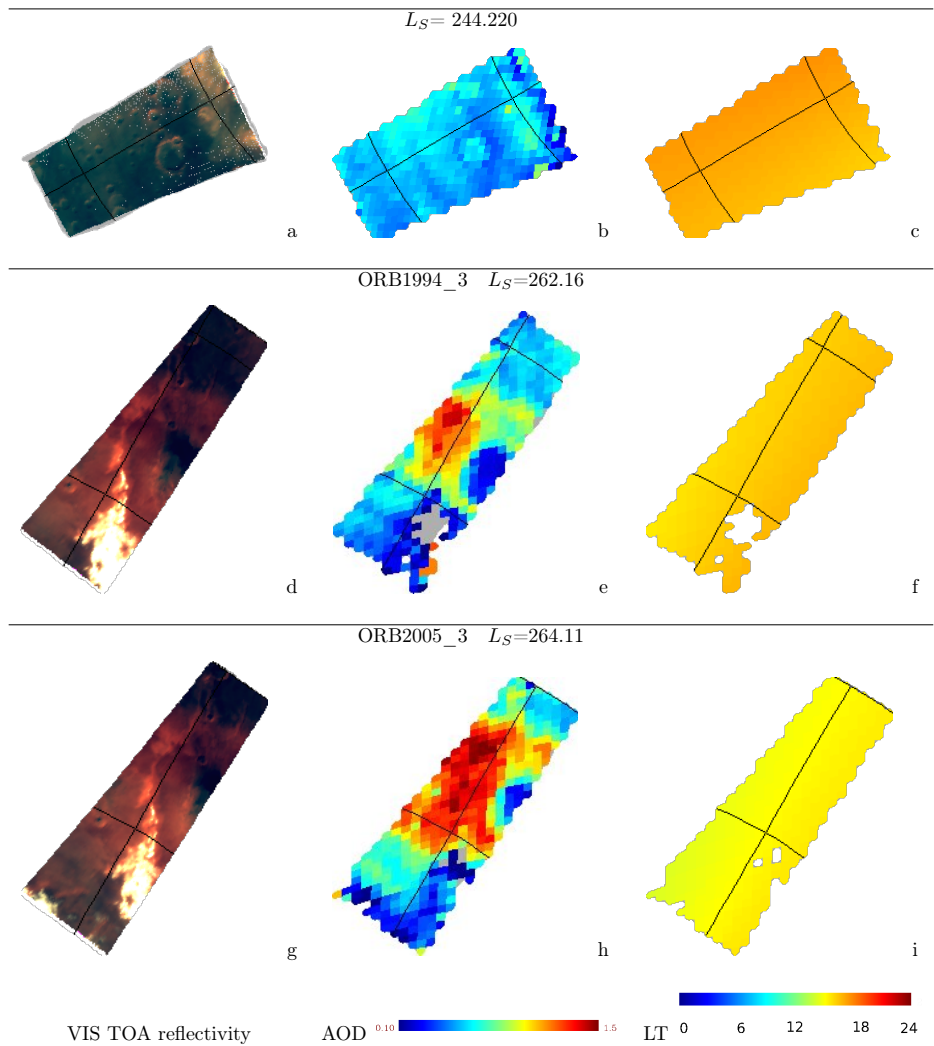


Figure 13: Same as Fig. 12 but with a selection of three local OMEGA observations concerning Unit 2 and 4a.

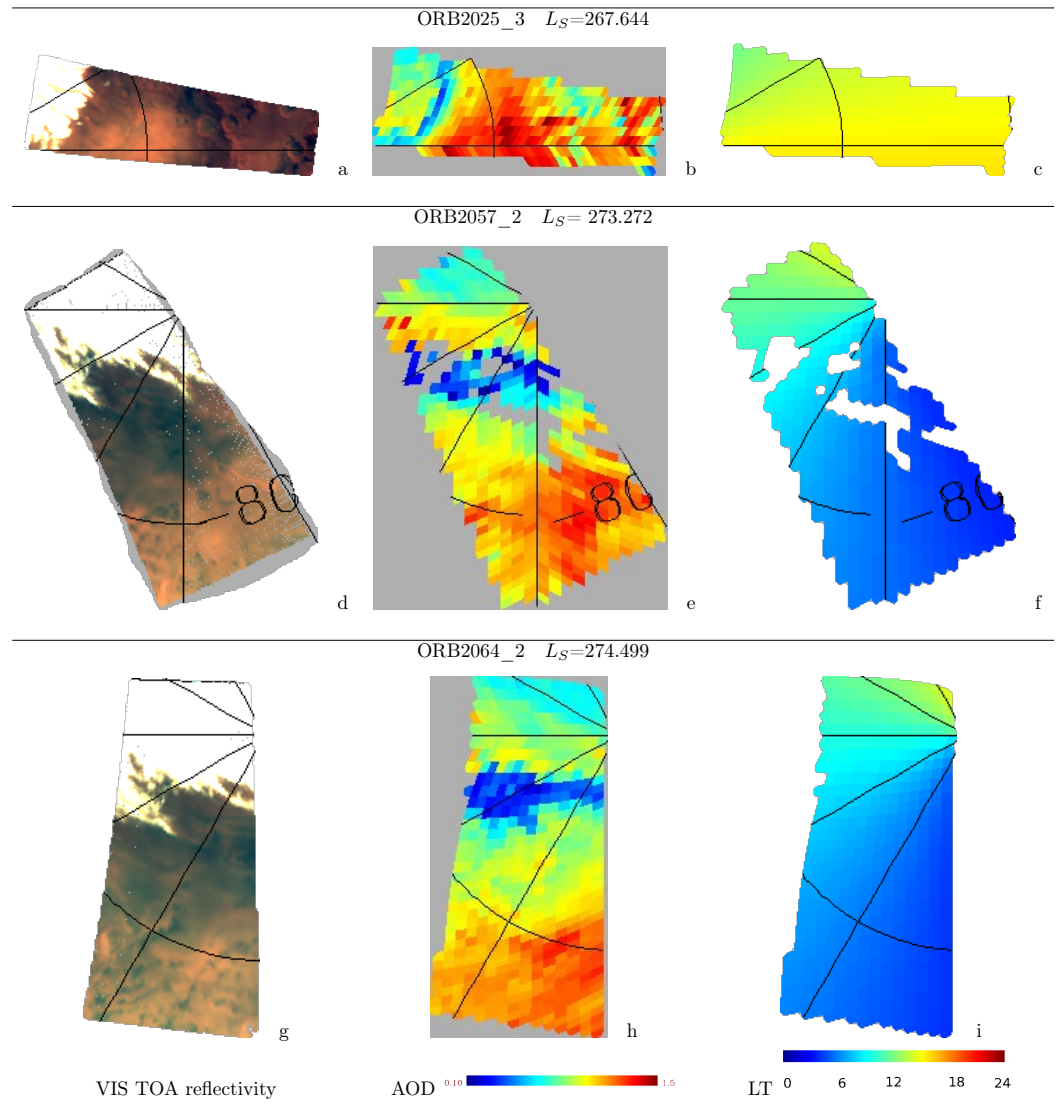


Figure 14: Same as Fig. 12 but with a selection of three local OMEGA observations concerning Unit 1.

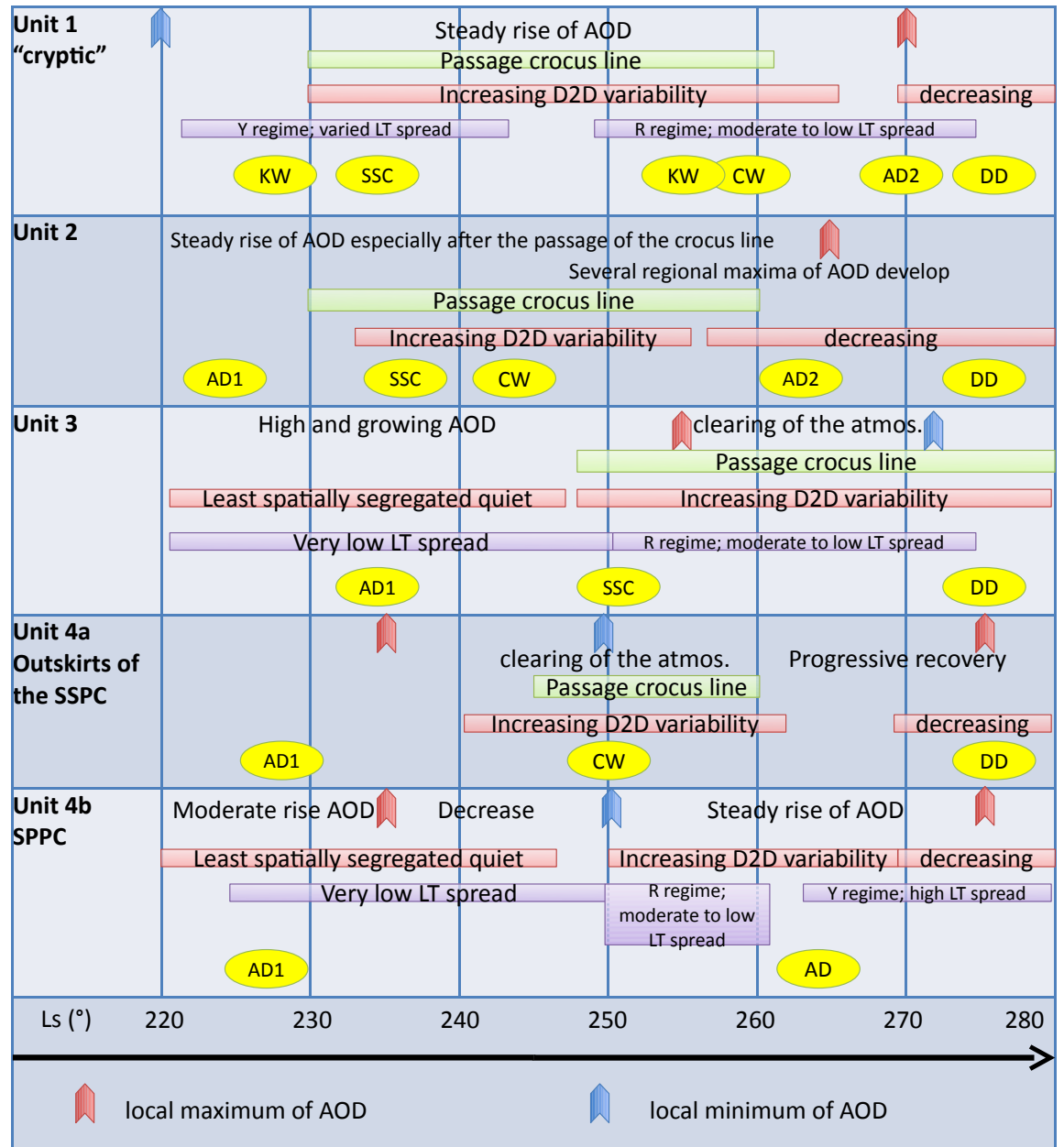


Figure 15: Synthetic view of the atmospheric dust activity in the high southern latitudes of Mars in mid-spring to summer. AOD Aerosol Optical Depth. AD1 and AD2: advection of dust respectively by high altitude return flows and cap winds (CW). KW: katabatic winds. DD: dust devils+convection in the boundary layer. SSC small scale convection in the transition zone. Y and R respectively yellow and red regimes. D2D: day to day.